Department of Applied Physics

Bio-Inspired Functional Materials

Hua Jin

Aalto University

DOCTORAL DISSERTATIONS

Aalto University publication series
DOCTORAL DISSERTATIONS 154/2012

Bio-Inspired Functional Materials

Hua Jin

A doctoral dissertation completed for the degree of Doctor of Science and Technology to be defended, with the permission of the Aalto University School of Science, at a public examination held at the lecture Hall D of Main Building of School of Science, Otakaari 1 (Espoo, Finland) on 20 November 2010 at 12 noon.

Aalto University
School of Science
Department of Applied Physics
Molecular Materials

Supervising professor
Acad. Prof. Olli Ikkala

Thesis advisor
Dr. Robin H. A. Ras

Preliminary examiners
Prof. Markus Linder, Aalto University, Finland
Prof. Orlando J. Rojas, North Carolina State University, USA

Opponent
Prof. Ingo Burgert, ETH Zürich, Switzerland

Aalto University publication series
DOCTORAL DISSERTATIONS 154/2012

ISBN 978-952-60-4874-1 (printed)
ISBN 978-952-60-4875-8 (pdf)
ISSN-L 1799-4934
ISSN 1799-4934 (printed)
ISSN 1799-4942 (pdf)
http://urn.fi/URN:ISBN:978-952-60-4875-8

Unigrafia Oy
Helsinki 2012

Finland

Publication orders (printed book):
hua.jin@aalto.fi

441 697
Printed matter

Aalto University

Abstract

Aalto University, P.O. Box 11000, FI-00076 Aalto www.aalto.fi

Author
Hua Jin

Name of the doctoral dissertation
Bio-Inspired Functional Materials

Publisher School of Science

Unit Department of Applied Physics

Series Aalto University publication series DOCTORAL DISSERTATIONS 154/2012

Field of research Molecular Materials

Manuscript submitted 11 September 2012 **Date of the defence** 20 November 2012

Permission to publish granted (date) 31 October 2012 **Language** English

☐ **Monograph** ☒ **Article dissertation (summary + original articles)**

Abstract

The thesis shows strategies how to learn from Mother Nature to make functional materials. Firstly, inspired by lotus leaf and water strider, superhydrophobic and superoleophobic surfaces are prepared from nanofibrillated cellulose aerogels. Furthermore, we explore potential applications of the superhydrophobic and superoleophobic materials for carrying cargo on liquid surfaces and continuous propulsion. Interestingly, the self-propelled locomotion has constant velocity and can last for prolonged time. This allows transduction of chemical energy into motility and could open doors for new generation of autonomous miniaturized soft devices. Subsequently, superhydrophobic and superoleophobic surfaces are made from silica aerogel, and the emphasis is on the damage resistance of superhydrophobicity and superoleophobicity. After mechanical abrasion with sandpaper, the superhydrophobicity and superoleophobicity retain. More interestingly, the contact angle hysteresis for water and oil decreases after abrasion with sandpaper.

The last part of the thesis is about bio-inspired tough materials from nanofibrillated cellulose and nanoclay. By a simple method of centrifugation, bulk nanocomposites are achieved that have a high work to fracture of 23.1 MJ/m^3 with high strain to failure of 36% under compression. Considering the simple preparation methods and bio-based origins of nanocellulose and clay, the tough material shows potential in applications for sustainable and environmentally friendly materials in construction and transportation.

Keywords nanocellulose, non-wetting, floatation, propulsion, toughness

ISBN (printed) 978-952-60-4874-1 **ISBN (pdf)** 978-952-60-4875-8

ISSN-L 1799-4934 **ISSN (printed)** 1799-4934 **ISSN (pdf)** 1799-4942

Location of publisher Espoo **Location of printing** Helsinki **Year** 2012

Pages 88 **urn** http://urn.fi/URN:ISBN:978-952-60-4875-8

Preface

The research in this thesis has been carried out in the Molecular Materials group, Department of Applied Physics in Aalto University School of Science. I am especially grateful to my supervisor, Acad. Prof. Olli Ikkala, not only for his support in research of sharing great ideas but also his encouraging attitudes and inspiration. I would like to give my special thanks to my instructor, Dr. Robin Ras who constantly shows me how to work as a scientist and responds fast on my questions and problems.

Before my master thesis, I never thought that I would have a doctor degree in science especially in Physics. My interests in science started from my master thesis under supervision of Markku Auer in Åbo Akademi. There, my work was about papermaking chemistry. I would not come to Molecular Materials group without help from Prof. Mika Lindén who gave me a chance to meet nanoscience and Prof. Janne Ruokolainen who gave me a chance for interview. My sincere gratitude goes to Prof. Anyuan Cao for his support during my visit in Beijing University. Prof. Abraham Marmur, Prof. Lars Berglund, Prof. Gero Decher, Prof. Janne Laine, Dr. Xuelin Tian, Dr. Andreas Walther, Dr. Ari Laiho, Dr. Jani Seitsnon, Enzheng Shi, Luhui Zhang, Mikael Ankerfors, Prof. Tom Lindström, Prof. Jouni Paltakari, and Hanna Pynnönen are thanked for collaboration.

I would express my appreciation to Marjo Kettunen and her true interest in research about cellulose affected me strongly.

Doing research in Molecular Materials group is enjoyable thanks to the inspiring, encouraging and enthusiastic working environment. Thanks to all past and current members for the contribution. Valuable conversation with Ying Tian, Hua Jiang, Miao Wang, Maoshuai He and Panu Hiekkataipale about science and life is really good refreshment during work. I wish to thank Susanna Junnila, Antti Nykänen, Antti Soininen, Juuso Korhonen, Henrikki Mertaniemi, Mika Latikka and Mikko Poutanen for their support related to devices and software.

I deeply indebted to Hongbian Li, Peixu Li, Zhen Li, Chunyan Ji, and Yuanyuan Shangguan for their help during my visit in Beijing University.

Thanks to Prof. Markus Linder and Prof. Orlando J. Rojas for their valuable time for pre-examination. I thank Benjamin Finley and Nonappa Nonappa for reading and correction.

The research in this thesis is funded by Academy of Finland (in part), TEKES-funded project Naseva, and EU FP7 SustainComp (in part).

Finally, many thanks go to my friends and family members for their support and encouragement. Thanks to my parents and parents in law for their constant support and love. Thanks to my husband for his love, encouragement and sharing of taking care of our kids. Warm thanks to my son Kangze for his inspiration and special “teaching” and my daughter Kangxin for her sweet words for encouragement.

Espoo, 26th August 2012
Hua Jin

我要感谢我的父母，自从我出生，给我无私的爱，也感谢他们一如既往的支持。要向教过我的所有老师和导师道一声感谢，特别是秦梦华和傅英娟老师。我也要感谢我的公婆，感谢他们对我学业的理解和支持。感谢我的舅舅，我生活中的良师益友。

感谢我的新老朋友们，在我大学，硕士和博士期间对我的帮助。田莹，少霞， 炳之，萍萍，聪聪，徐谦，宋涛，程久军，洪燕，蒋华，陈娅，王苗，田雪林，李娟，王枫，何茂帅，董珊，王爽，晓春，葛艳玲，李敏，李畅，增森，秀强，云静，雪红，张丽，感谢你们在学习，工作和生活中的帮助。

最后感谢我的爱人吴红卫，感谢他几年来风雨相伴，给我一个温暖的家。康康, 很高兴你和妈妈分享成长的快乐和烦恼，谢谢你用纯真的办法来帮妈妈解决问题。开心, 你是我们家快乐的种子，你和哥哥的微笑是妈妈动力的源泉。康康和开心，你们让爸爸妈妈的生活更精彩！

感谢所有帮过我和我们家的朋友！

Contents

Publications I-IV

Thesis publications

I. **Jin, H.,** Kettunen, M., Laiho, A., Pynnönen, H., Paltakari, J., Marmur, A., Ikkala, O., and Ras, R.H.A. Superhydrophobic and Superoleophobic Nanocellulose Aerogel Membranes as Bioinspired Cargo Carriers on Water and Oil, Langmuir 27 (5), 1930-1934 (2011)

II. **Jin, H.,** Marmur, A., Ikkala, O., and Ras, R.H.A. Vapour-Driven Marangoni Propulsion: Continuous, Prolonged and Tunable Motion, Chemical Science 3, 2526-2529 (2012)

III. **Jin, H.,** Cao, A., Shi, E., Seitsonen, J., Zhang, L., Ras, R.H.A., Berglund, L.A., Ankerfors, M., Walther, A., and Ikkala, O. Ionically Interacting Nanoclay and Nanofibrillated Cellulose Lead to Tough Bulk Nanocomposites by Forced Self-Assembly, under revision for Journal of Materials Chemistry B

IV. **Jin, H.,** Tian, X., Ikkala, O., and Ras, R.H.A., Preservation of Superhydrophobic and Superoleophobic Properties upon Wear Damage, submitted to ACS Applied Materials & Interfaces

Author's contribution

I. The author participated in planning and implementation research. The author carried out most of the experimental work except that Dr. Ari Laiho did the drag reduction part and Dr. Robin Ras did the plastron part together with the author. The author wrote the first version of the manuscript.

II. The author participated in planning and implementation the research. The author carried out most of the experimental work. The author wrote the first version of the manuscript.

III. The author designed the experiments and completed most of the experimental work except that Enzheng Shi did SEM and Dr. Jani Seitsonen did TEM. The author wrote the first version of the manuscript.

IV. The author participated in planning and implementation the research. The author carried out most of the experimental work except that Dr. Xuelin Tian helped to complete and edit the abrasion video. The author wrote the first version of the manuscript.

Other featured publications

I. **Jin, H.,** Pääkkö, M., Ikkala, O., and Ras, R.H.A. Liquid-Repellent Material, Patent Application FI 20095752, PCT/FI2010/050575, July 2, 2009

II. Granström, M., Kettunen née Pääkkö, M., **Jin, H.,** Kolehmainen, E., Kilpeläinen, I. and Ikkala, O., Highly water repellent aerogels based on cellulose stearoyl esters**,** Polymer Chemistry 2, 1789-1796 (2011)

List of symbols and abbreviations

3D	three-dimensional
CA	contact angle
CBD	cellulose binding domain
C-NFC	cationic nanofibrillated cellulose
CNC	cellulose nanocrystal
CVD	chemical vapor deposition
FE-SEM	field emission scanning electron microscopy
FTCS	(tridecafluoro-1,1,2,2-tetrahydrooctyl)trichlorosilane
HFB	hydrophobin
MTM	montmorillonite, nanoclay
LbL	layer-by-layer deposition
NFC	nanofibrillated cellulose, native microfibrillated cellulose
PVA	polyvinyl alcohol
SEM	scanning electron microscopy
TEM	transmission electron microscopy

1. Introduction

Biological materials observed in nature have exciting properties such as self-assembly, self-cleaning, self-healing, and combinations of toughness, strength, and stiffness. They inspire and attract scientists from different fields to learn the complex systems and make artificial materials and systems that mimic the structures and functions of natural materials. In this thesis, we focus on superhydrophobic, superoleophobic, and self-cleaning materials in Chapters 2 and 3 and tough nanocomposite materials in Chapter 4.

1.1 Bio-Inspired Superhydrophobic and Superoleophobic Materials

The specific surface wetting properties of several plants and animals have attracted considerable interest due to the potential to develop novel coatings with special wettability. Classic examples are Lotus leaves (Fig. 1.1 A, B) and the legs of the water strider (Fig. 1.1 C, D), where the static contact angle (CA) for a water droplet is in excess of 150°, indicating superhydrophobic behavior. *[1-7]* The phenomenon has been explained by a combination of low surface energy coatings and a hierarchical surface topography. So far, numerous superhydrophobic surfaces based on synthetic materials have been developed by understanding the prerequisites of low surface energy, and roughness *[7]*. Most of these synthetic surfaces are prepared by lithography, etching, sol-gel processes, chemical vapor deposition (CVD), nanoparticles, and electrospinning. Strictly, superhydrophobicity requires small contact angle hysteresis between the advancing and receding CAs, whereupon water droplets roll off even at small tilting angles of the substrate. More recently, there have been efforts to achieve CAs in excess of 150° even for oil-like liquids, *[8, 9]* i.e. superoleophobicity. However, oils have a surface tension of only a fraction of that of water. Thus developing superoleophobic materials is more challenging than superhydrophobic materials because it involves coatings with extremely low surface energy and carefully designed surface topography.

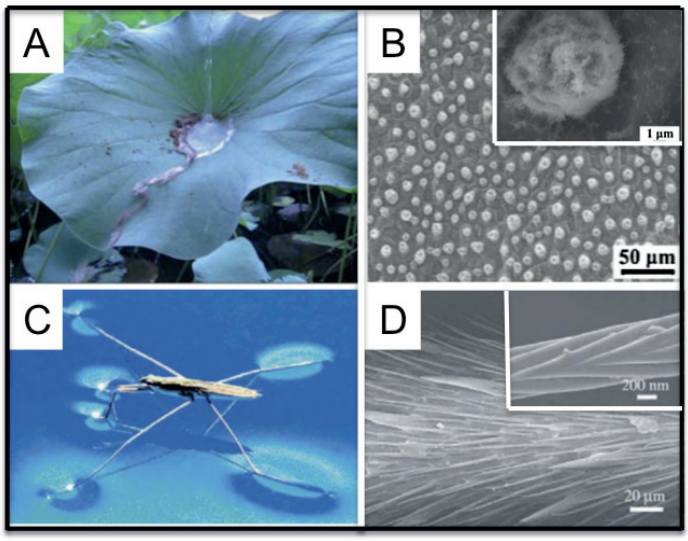

Figure 1.1 Photo of Lotus leaf (A) and water strider (C). (B) and (D) show SEM of the surfaces of Lotus leaf and water strider's leg, correspondingly. The insets in (B) and (D) show the secondary structures, indicating structural hierarchies. (Reprinted with permission from Ref [7] Copyright © 2011, Elsevier)

Inspired by water striders floating on water surface due to their superhydrophobic legs, in Chapter 2, we demonstrate that superhydrophobically and superoleophobically modified nanofibrillated cellulose (NFC) aerogels float on water and oils. In addition, the aerogels are capable of supporting weights of nearly three orders of magnitude larger than the weights of the aerogels themselves on water and oil surfaces. We foresee applications including buoyant, gas permeable, and dirt-repellent coatings for miniature sensors and other devices floating on generic liquid surfaces. The gas permeability of the superamphobic NFC aerogel membrane allows vapor of carried fuel to permeate into the liquid that the membrane floats on, thus creating a surface tension gradient. Very interestingly, a continuous self-propulsion is induced by the surface tension gradient under the membrane from a vapor-driven Marangoni effect. The steady velocity is achieved through a continuous supply of fuel vapor that asymmetrically lowers the surface tension of the liquid below the aerogel membrane, combined with the spontaneous recovery of the surface tension after the floating device has passed due to fuel evaporation.

Applications of superhydrophobic and superoleophobic surfaces are limited due to their low resistance to damage. Damage resistant superhydrophobicity and superoleophobicity have been developed based on self-healing or preservation of topography*[9-11]*. A priori it would be

expected that abrasion would reduce superhydrophobicity and superoleophobicity due to wearing of the surface patterns or/and surface coatings. Also surface contamination during abrasion may lead to undesired pinning of water droplets. We come up new concepts for damage resistant superhydrophobicity and superoleophobicity, so that the favorable wetting properties could be retained even after mechanical damage. We demonstrate damage-resistant superhydrophobicity and superoleophobicity in Chapter 3.

1.2 Bio-inspired Materials Mimicking Nacre and Bone

Nacre and bone (Fig. 1.2) are natural composites showing extremely high toughness in combination with strength and stiffness. They are hybrid materials combining inorganic and organic components *[12]*. Nacre is composed of more than 95 % of self-assembled plate-like inorganic component and only a small amount of organic component, leading to an extremely high toughness that is difficult to replicate with artificial materials *[12-14]*. In bone, the structure involves seven levels of highly sophisticated hierarchies, based on minerals and collagen fibrils. The collagen fibrils, which consist of an assembly of collagen chains, are the main building blocks of the bone matrix. Hydroxyapatite minerals align in the gap between collagen fibrils and form lamellar structures within the collagen fibrils, thus promoting the high toughness of bone *[13, 15-19]*. It has been noted that bone has remarkable inelastic strain, which makes it adapted better to the environment when load is applied, thus suppressing tendency for catastrophic fracture. Learning from nacre and bone, the hierarchical structure (Fig. 1.2) and the interaction between inorganic component and organic component are important for designing tough materials with good ways to dissipate energy.

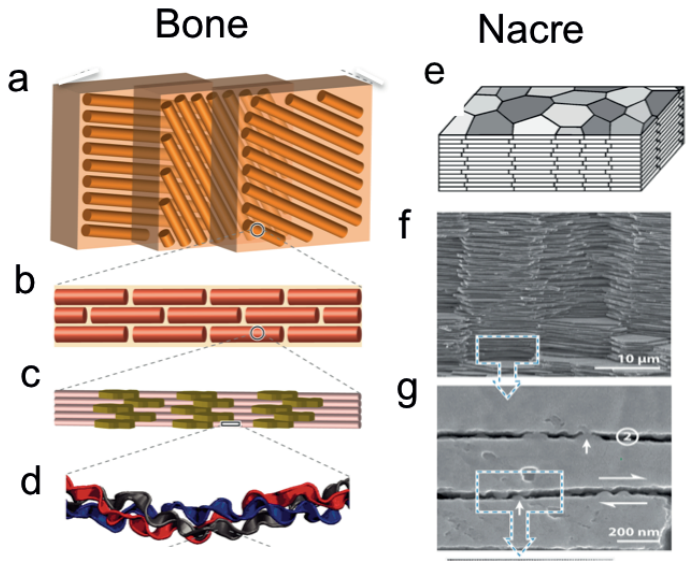

Figure 1.2 Hierarchical structures in bone (a-d) and nacre (e-g) *[17, 20]*. (a) Fiber patterns with dimension of ~ 50 mm. (b) Fibril arrays in the range of ~ 10 mm. (c) Mineralized collagen fibrils in the range of ~ 300 nm. (e) The brick and mortar structure in the range of mm. Each platelet layer has ~ 0.5 µm thickness and ~ 8 µm length in (f) and (g).

Several approaches have recently been developed for strong and stiff biomimetic composite films; these approaches will be discussed later in more detail. However, it has remained challenging to achieve high toughness using simple processes especially for bulk materials. We demonstrate in Chapter 4 that ionically interacting cationic nanofibrillated cellulose (C-NFC) and anionic nanoclay, i.e. montmorillonite (MTM) pack using a simple centrifugation process to achieve 3D bulk materials showing local self-assemblies. For the composite with MTM/C-NFC 63/37 w/w, we show compression strength of 76 MPa, high compressive strain to failure of 36%, and work to fracture of 23.1 MJ/m^3. Considering the simple preparation method and bio-based origin of NFC, the tough bulk nanocomposites are good candidates for sustainable and environmentally friendly materials in construction and transportation.

2. Superhydrophobic and Superoleophobic Aerogels for Cargo Carriers and Continuous Propulsion

2.1 Background

2.1.1 Nanofibrillated Cellulose

Considerable effort has been spent searching for sustainable polymers for bulk and functional materials. Cellulose is the most abundant polymer, being the main constituent in plant cell walls. Furthermore, cellulose is regarded as environmentally friendly, renewable, biocompatible and biodegradable. Therefore native nanocellulose-based materials have attracted considerable interests as sustainable materials *[21-26]*. Recently, there has been a significant development in processing nanocellulose either by mechanical treatment and/or by chemical treatment (Fig. 2.1) *[24-35]*. It has to be noted that nanocellulose has extraordinary mechanical properties due to its native crystalline structure, as derived from the high axial crystal modulus of cellulose I of ca. 140 GPa *[31]*.

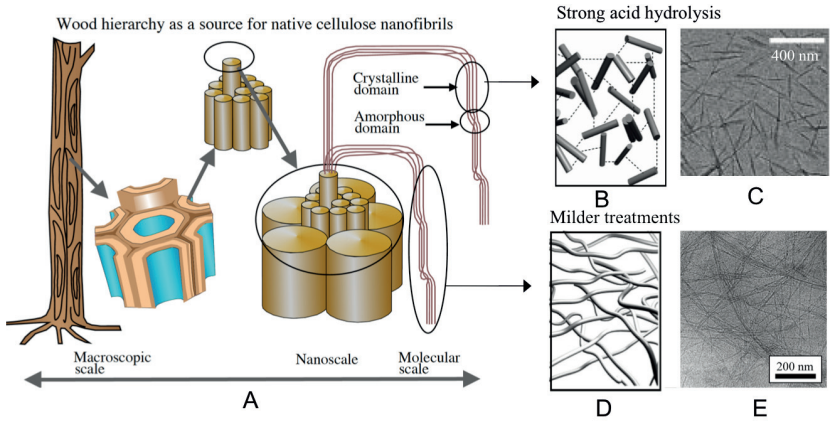

Figure 2.1 (A) A simplified scheme of the hierarchical structures in wood and plants to extract native nanocelluloses. Scheme (B) the rod-like cellulose nanocrystal (CNC) structure after hydrolyzing the amorphous domains with a strong acid and (C) TEM image for short rod-like CNC from Cellulose I by acid hydrolysis after removing amorphous regions *[25]*. (D) shows the scheme for long and entangled nanofibrillated cellulose (NFC) from milder treatment where the connecting amorphous domain remain. (E) Cryo-TEM image of 2% w/w NFC gel after refining, enzymatic hydrolysis, and homogenization processes, showing a fibrillated network of nanoscale fibrils *[22]*.

There are two main classes of nanocellulose. The first class is short rod-like cellulose nanocrystals usually denoted as CNC. It is obtained from cellulose through strong acid hydrolysis by hydrolyzing the disordered or para-crystalline regions in cellulose, leaving the crystalline regions intact (Fig. 2.1 B, C)*[26]*. Technological applications of CNC have been pursued from acid-assisted degradation of cellulose fibers from wood pulps followed by sonication treatments. The other main class of nanocellulose is nanofibrillated cellulose (NFC) or sometimes denoted as microfibrillated cellulose (MFC), which contributes much for functional materials in Chapters 2 and 4. NFC is cleaved from wood cell walls mainly by mechanical treatment of homogenization, grinding, or sometimes with the help of chemical pre-treatment, or so-called TEMPO-oxidation. *[22, 25, 29, 31]* The mechanical/ chemical treatment does not remove amorphous regions within the fringed fibrils, thus the cellulose structure retain, resulting in long and entangled NFC nanofibers. NFC nanofibers have an average diameter of several nanometers and length of several micrometers, as illustrated in Fig. 2.1 E. It can be seen that there are not only individual nanofibers but there may be also fibril bundles due to incomplete disintegration of fibrils. Considering the abundant natural source, biocompatibility, and high mechanical properties *[35],* NFC is a good candidate for different functional materials and composites.

2.1.2 Aerogels

Aerogels are materials obtained from well-controlled drying processes to maintain highly porous structures and networks by replacing the liquid medium in the wet gels with gas or air, as shown in Fig. 2.2. The air- or gas-filled network structure can reach very low densities down to ca. 10 mg/cm^3, high porosities in excess of 95%, and high surface areas. Since the first invention of aerogels *[36],* numerous types of aerogels have been explored, such as silica gels, metal oxides, cross-linked polymers, regenerated cellulose, and carbon-based materials.*[37-49]* Aerogels have attracted intense interests for lightweight construction, thermal and acoustic insulation, membranes, separation, chemical analysis, catalyst support, sensing, energy technologies, and energy absorption *[23, 37, 44, 48-60]*. Our emphasis is in NFC and silica aerogels. NFC aerogel is typically obtained by freeze-drying a NFC hydrogel, while silica aerogel is usually obtained from a wet silica gel by a sol-gel process combining supercritical drying. Typical aerogels have suffered from brittleness, but very recently concepts for ductile and flexible aerogels have been shown, where in particular carbon nanotube aerogels, native nanofibrillated cellulose and bacterial cellulose aerogels are relevant *[23, 56, 61, 62]*. Several concepts

have been introduced to functionalize NFC aerogels *[23, 50, 60, 64]*. Another problem is that most aerogels are sensitive to water or other liquids and this limits their applications. This chapter we focus on superhydrophobic and superoleophobic NFC aerogels and their potentials in floatation and self-propulsion. Non-wetting properties of modified silica aerogels will be discussed later in Chapter 3.

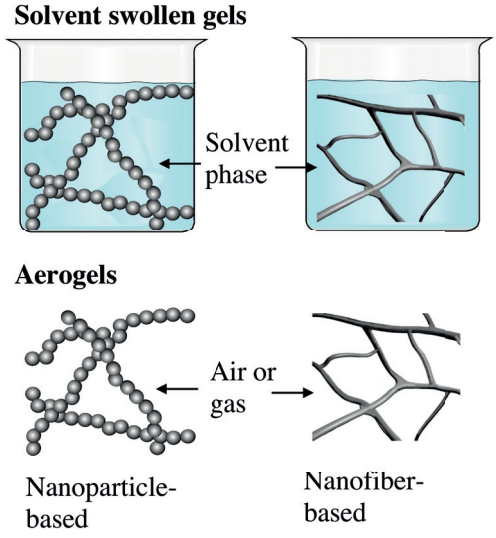

Figure 2.2 Schemes for aerogel processes from wet gels to aerogels. The left hand side is a scheme for the nanoparticle-based materials (such as silica aerogels) and the right hand side is a scheme for the nanofiber-based materials (such as NFC aerogels).

2.1.3 Preparation of Superhydrophobic and Superoleophobic Surfaces

Surfaces and materials that repel liquids are of great interest due to their potential for self-cleaning, anti-fouling, anti-icing and applications that require drag reduction *[65-67]* such as for ships and boats *[68, 69]*. There have been significant developments in superhydrophobic surfaces that repel water. It has been found that roughness or hierarchical structures combining coatings with low surface energy are the prerequisites for designing and producing superhydrophobic surfaces. The problem is that most superhydrophobic surfaces will be contaminated by organic liquids and therefore there is a desire for superoleophobic surfaces that repel also organic liquids. However, superoleophobic surfaces are more challenging to produce because organic liquids have a surface tension that is only a fraction of that of water. Very recently, re-entrant curvature has been proposed for designing superoleophobic surfaces *[8]*. There, a spacing ratio $D^* = (R+D)/R$ (see Fig 2.3) is reported to directly affect the wetted surface

fraction to achieve superoleophobic surfaces with re-entrant curvature, the spacing ratio D* >> 1 is required.

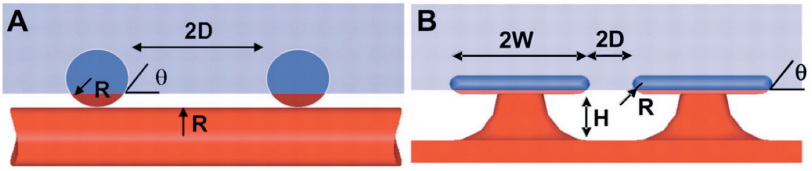

Figure 2.3 The critical role of re-entrant curvature for superoleophobicity. The drawings highlight the formation of a composite interface on surfaces with re-entrant topography (for both fibers and micro-hoodoos). The geometric parameters R, D, H, and W characterize these surfaces (R is the radius of the fibers and D is the average edge-to-edge spacing between two fibers. W is hoodoo spacing and H is the hoodoo height.). The blue surface is wetted while the red surface remains non-wetted when in contact with a liquid whose equilibrium CA is θ (< 90°). (Reprinted from Ref *[8]* with permission from AAAS)

2.1.4 Bio-Inspired Concepts for Floating

The source of inspiration regarding floatation is water-borne insects. For example, the Gerridae family of water striders has a characteristic weight of ca. 10 mg, length of ca. 10 mm, and six legs that are covered by a dense set of micron scale hairs (Fig. 2.4 A), i.e. setae, that have nanoscale grooves and low surface energy coatings, thus showing structural hierarchy. Therefore the legs have a water CA of 167°, leading to superhydrophobicity and floatation on water due to surface tension forces. *[5, 70]* In rough analogy, our NFC membranes show structures at several length scales from nanometer scale individual NFC fibrils up to micronscale nanofibrous aggregates (Fig 2.4 B). The native NFC fibers are cleaved from the self-assembled hierarchy of macroscopic cellulose fibers *[22, 23],* whereupon they form aqueous hydrogels, and are further freeze-dried for highly porous aerogels. Unlike most aerogels, the native NFC aerogels are not brittle *[23]* and the mechanical properties of individual NFCs are expected to approach those of steel due to the hydrogen bonded parallel cellulose chains. Here the aerogels are fluorinated by using trichlorosilanes by CVD. Without the fluorination treatment, a water droplet becomes immediately absorbed within an aerogel without any measureable CA. In contrast, for the fluorinated aerogel, a CA of 160° is observed for water. Even more interestingly, high CA of 153° is observed for paraffin oil. Overhang structures promote superoleophobicity *[8],* and the present concept allows a particularly simple and scalable approach for overhang structures caused by highly porous network structure in NFC aerogel.

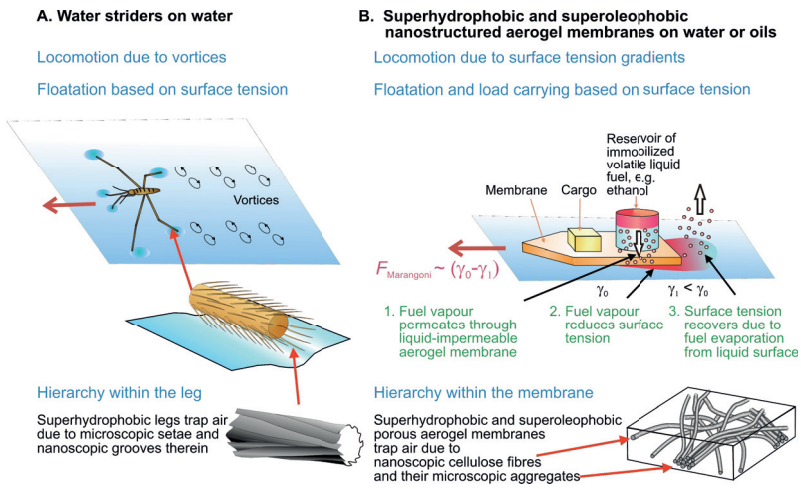

Figure 2.4 Schematics of locomotion on water and oil. (A) Water striders provide an example of insects capable of floating on water based on surface tension. The superhydrophobic legs contain surface functionalized microscopic fibers (i.e. setae) containing nanoscale surface topography, which allow high CA for water. The locomotion is mechanically induced based on vortices. (B) Schematics for an object capable of locomoting and floating on water and oil due to surface tension, based on fluorinated NFC aerogel membrane. As in water striders, also in the aerogels the topography for liquid repellency is induced by fibers, but in this case the fibers form mechanically robust entangled networks. Steady-state propulsion is achieved, as the aerogel membranes are permeable to gases and impermeable to water and oil. This allows evaporation from volatile fuel (e.g. ethanol or pentane) through the membrane to allow surface tension gradients underneath the object to transduce chemical energy from the fuel into locomotion.

2.1.5 Bio-Inspired Concepts for Continuous Locomotion

Water striders locomote mechanically, based mainly on vortices instead of surface energies *[72, 73]*. In contrast, some insects exhibit burst-like Marangoni effects (interfacial motion induced by surface tension gradients) upon excretion of a surfactant to escape from predators *[72-74]*. However, the surfactant release does not allow steady-state locomotion, as the surface tension gradients quickly decay by equilibration of the interfacial surfactant concentration. Instead, we use vapors evaporating from volatile liquid fuels permeating across floating liquid-impermeable membranes to modify the surface tension *[75]*. If the fuel reservoir is asymmetrically located on the membrane, this leads to a net surface energy gradient on the liquid beneath the membrane and subsequent Marangoni propulsion. The vapors dissolved in the upper layers of the liquid ultimately evaporate, thus causing the recovery of the original surface tension, which maintains the surface energy gradient constant, and causes locomotion in a steady state.

In addition, steady Marangoni locomotion for a prolonged time requires dispensing of fuel at a low and steady rate. The low supply rate is critical, especially for miniature floating objects, as otherwise a large mass of liquid fuel would need to be taken onboard, thus compromising the load carrying capacity for useful cargo such as electronic devices. Here we propose to supply vaporized fuel for steady Marangoni propulsion, firstly because the supply of fuel vapor is autonomous and at a steady rate as it is controlled by the evaporation process, and secondly because the amount of fuel molecules in the vapor (although significantly lower than in liquid fuel) is sufficiently high to modify the surface tension of liquids. The novel concept of gas-permeable and liquid-impermeable membranes for locomotion is schematically shown in Fig. 2.4 B.

2.2 Experimental and Methods

2.2.1 Preparation of Nanofibrillated Cellulose Aerogel

The pulp used in refining to prepare NFC was a commercial never-dried ECF-bleached birch kraft pulp from UPM-Kymmene, Finland. The pulp suspension was first diluted to a 3% consistency and NFC were disintegrated using an ultra-fine friction grinder (Masuko Supermasscolloider®, model MKZA 10-15J). The grinder consists of lower rotating and upper stationary SiC grinding stones (gap 100 μm). During the grinding, the power consumption was kept at levels 3.2–3.8 kW (total energy consumed 15 kWh/t). The pulp suspension was recirculated into the grinder five times. The grinding leads to hydrogels due to disintegration of the macroscopic cellulose fibers into NFC. Water was added during the grinding process, leading to a NFC hydrogel with final solids content of 1.3%.

Drying of native NFC hydrogels into aerogel membranes without essential collapse has been described before *[23]*. In order to make the NFC well dispersed, the hydrogel was magnetically stirred for one day before use. The mould used to prepare the aerogel membranes was a press-to-seal silicone isolator (Grace Bio-Labs, thickness of 0.5 mm, diameter of 20 mm) on a glass slide. The mould was carefully filled with the NFC hydrogel. Next, the mould with hydrogel was transferred in a vacuum oven at room temperature. When the hydrogel sample was exposed to vacuum, it quickly became frozen and the frozen water was removed by sublimation in the vacuum oven. The drying was stopped when the pressure reached $3x10^{-2}$ mbar.

A piece of the aerogel membrane was placed in a 30 mL glass bottle. 200 µL (Tridecafluoro-1,1,2,2-tetrahydrooctyl)trichlorosilane (FTCS) (97%, ABCR) was inserted in another 2 mL glass bottle. The 2 mL glass bottle containing FTCS was placed inside the above-mentioned 30 mL bottle. This "bottle-in-bottle" setup was designed to avoid direct contact between the aerogel membrane and liquid FTCS. Finally, the 30 mL bottle was sealed with a cap and placed for 2 h in an oven at 70 °C. To remove the unreacted silanes, the aerogel was kept in a vacuum oven until the vacuum level reached $3x10^{-2}$ mbar or less.

2.2.2 Scanning Electron Microscopy (SEM)

JEOL JSM-7500F field emission scanning electron microscope (FE-SEM) was used to characterize the nanostructures and to observe the porosity in NFC aerogel membranes. In order to avoid charging, the membranes were sputtered with gold under vacuum conditions at 20 mA for 1 min.

2.2.3 Wetting Characterization

The wetting properties of the aerogel membranes were characterized by CAM 200 Optical Contact Angle Meter (KSV Instruments). In the static mode, droplets of Milli-Q water, paraffin oil (University Pharmacy Ltd; Finland, used as received) or mineral oil (Teresstic, grade ISOV6150, used as received) were placed on the surface of the fluorinated membrane at room temperature. The droplet volume for water was 10 µL and for oils 5 µL. The CA values were calculated using the contact angle meter software based on the shape of the droplet in the image. CA values for both water and oil were recorded for two minutes and remained stable. To obtain further information about the wetting properties, images were taken when the fluorinated aerogel surface was tilted at 90° and 180° for both water and oil. The droplets at these angles remained stable during the 2 min measurement.

2.2.4 Load Carrying Experiments and Continuous Propulsion

A fluorinated aerogel membrane with diameter of 19 mm, thickness of 0.5 mm and mass of 3.0 mg was placed on a bath filled with Milli-Q water or bath filled with paraffin oil. A ruler was placed parallel to the bath. Loads were carefully added on top of the floating aerogel membrane. The total mass of the weights before the aerogel sank was measured. Contrast illumination allowed imaging the meniscus of the dimple.

To show steady-state locomotion, a volatile fuel reservoir was placed on the upper surface of the fluorinated aerogel membranes. The fuel reservoir consists of a plastic cup containing paper tissue with a few drops

of volatile liquid fuel, such as ethanol in the case of locomotion on water. The cup was placed on the rear of the vessel upside down to let the ethanol evaporate through the aerogel membrane (see later Fig. 2.7 B) to cause surface tension gradients below the membrane in order to move the vessel forward. This concept was also used to transport working electronic devices on water. Similar locomotion was realized for the aerogel membrane floating on paraffin oil using pentane as the fuel.

2.3 Results and Discussion

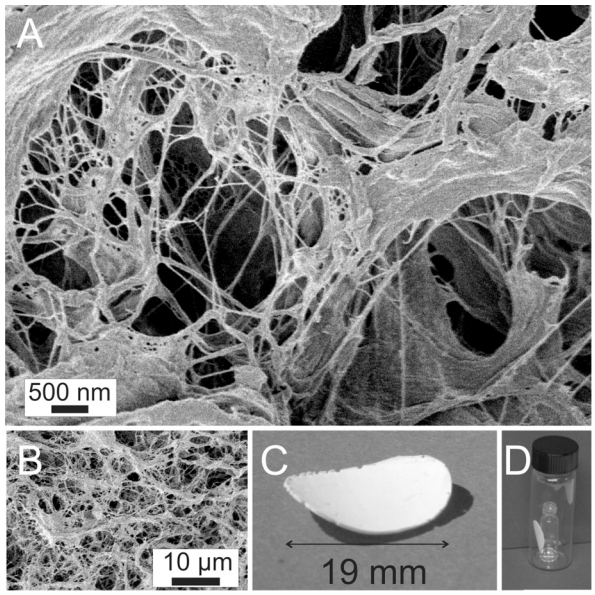

Figure 2.5 (A+B) Scanning electron micrograph of native NFC aerogel structure with robust network structuring at several length scales due to individual NFC and their aggregates. (C) Photograph of a NFC aerogel membrane. (D) Bottle-in-bottle setup for fluorination by CVD.

Mechanically robust nanocellulose aerogels with a mass of 3.0 mg, diameter of 19 mm and thickness of 0.5 mm are prepared by vacuum freeze-drying (Fig. 2.5 C). The resulting density is 0.02 g/cm^3 and the resulting porosity is 98.6%. The aerogels were fluorinated with trichlorosilanes using chemical vapor deposition (CVD) in a "bottle in bottle" set up as is shown in Fig. 2.5 D. The unmodified aerogel contains free hydroxyl groups on the surface, which react with trichlorosilanes to form a covalent Si-O bond. There are two advantages of the CVD bottle-in-bottle setup. Firstly, it avoids direct contact of the aerogel with the liquid fluoro-surfactant. Secondly, it reacts at low temperature (70°C) so that the inherent structures and properties of cellulose aerogel do not get damaged. Without the fluorination treatment, a water droplet becomes immediately absorbed within an aerogel without any measureable contact angle. In

contrast, the fluorinated aerogel has contact angles of 153° and 160° for paraffin oil (Fig. 2.6 A) and water respectively (Fig. 2.6 B), indicating superoleophobicity and superhydrophobicity.

The superhydrophobicity and superoleophobicity helps the membrane to achieve floating and load carrying capability. The load carrying capability of a fluorinated aerogel membrane on oil and water were inspected (Fig. 2.6 A, B) *[50,71]*. On oil in Fig. 2.6 A, an aerogel membrane with a mass of 3.0 mg and diameter 19 mm could carry a load of 960 mg. It made a dimple on oil surface; the edge of the aerogel membrane at its deepest point was 2.7 mm below the free liquid surface and the central part of the aerogel membrane reached a dimple depth of 4.3 mm. Correspondingly in Fig. 2.6 B, on water the aerogel membrane could carry a load of 1658 mg; the edge of the aerogel membrane at its deepest point was 3.7 mm below the free water surface and the central part of the aerogel membrane was 4.6 mm below the free water surface. The overview of a loading-carrying membrane floating on water is shown in Fig. 2.6 C.

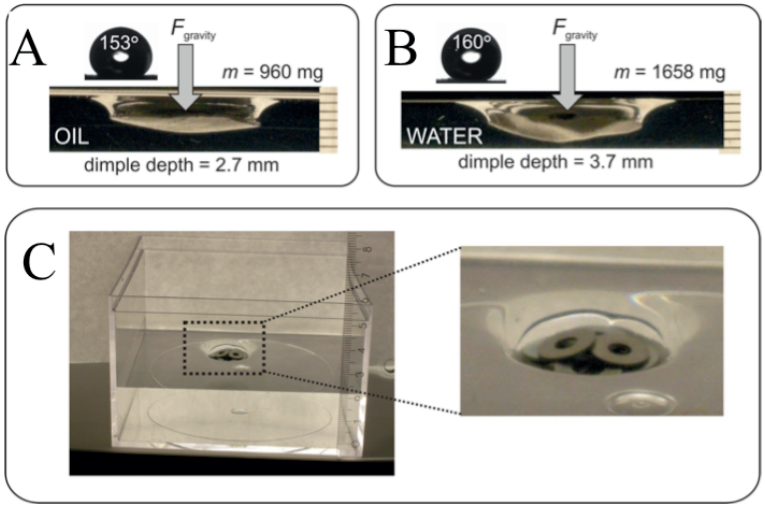

Figure 2.6 Floatation and load carrying on oil and water based on fluorinated NFC aerogel membrane. (A, B) CAs of the membrane for paraffin oil and water. (Bottom) Side view photographs of aerogel load carriers on paraffin oil and water at maximum supportable weight showing the dimple. Contrast illumination allows visualization of the menisci. The units in the scale bars on the right are in mm. (C) An overall figure on load-carrying membrane on water.

The cellulose aerogel is a solid material with an open porous structure as is shown in Fig. 2.5 A and B, and it allows permeation of gases. We demonstrate the gas permeability by using a pH indicator paper (Fig. 2.7). Here we encapsulate the indicator paper between fluorinated aerogel membranes, and expose it to a vapor of HCl. The pH indicator paper

rapidly changes colour, which demonstrates that HCl vapor has diffused through the aerogel. The aerogel thus acts as a membrane that is permeable for gases and vapors, but impermeable for liquids.

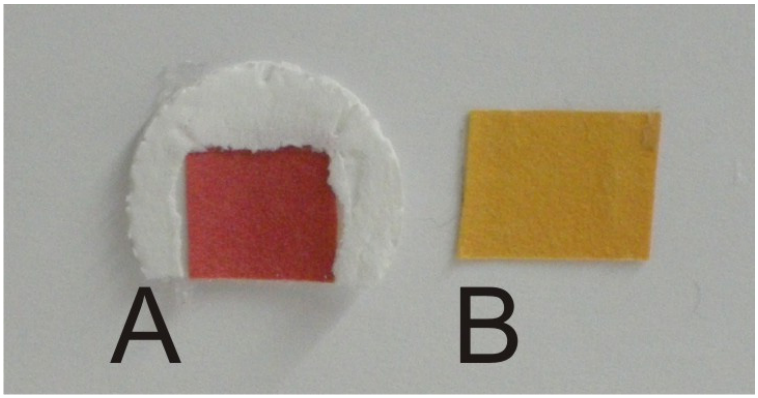

Figure 2.7 Gas permeability of the fluorinated aerogel membrane. (A) A piece of pH indicator paper is encapsulated between two fluorinated aerogel membranes, and subsequently exposed to HCl vapor. Upon exposure, the pH indicator rapidly changes from yellow to red (in the photograph we removed one aerogel membrane for clarity), showing that HCl vapor rapidly passes through the aerogel. (B) The original pH indicator paper is shown on the right.

Relevant to the locomotion concept is the porosity of the fluorinated NFC aerogel membranes that allows vapor permeation through the membrane, while oil or water is prevented from permeating. Fig. 2.4 B shows a scheme of a centimeter-sized vessel prepared from a fluorinated aerogel membrane and a plastic fuel reservoir open at the bottom, containing a paper tissue to immobilize a few drops of ethanol as a volatile liquid fuel. The vessel with its fuel reservoir is placed on water where it floats due to surface tension. The ethanol evaporates through the aerogel membrane, and as the cup was positioned asymmetrically at the rear of the vessel, the surface tension of water (σ_{water}) behind the vessel decreases due to the formation of a water-ethanol solution near the water surface (at 20°C σ_{water} = 72.8 mN m^{-1}, $\sigma_{ethanol}$ = 22.1 mN m^{-1}). The gradient of surface tension between the back of the vessel and its front drives the locomotion. Once the vessel locomotes, the ethanol at the end evaporates and the surface tension of pure water is gradually restored. Unlike other Marangoni propulsion mechanisms incorporating burst-like release of liquid or solid surfactants, in the present case the supply of ethanol is steady and controlled by the evaporation and transport through the aerogel membrane. Also, the evaporation of ethanol from the water surface allows continuous locomotion due to restoration of the water surface tension. Thus, a novel type of steady Marangoni locomotion is presented.

In a typical experiment, evaporation of as little as 25 μL of ethanol allowed a range of 74 m during nearly one hour for a centimeter-sized vessel. It may be of interest to note that this corresponds to a fuel consumption of 33 mL per 100 km. The vessel was designed to perform a circular trajectory, which allowed to monitor the time of each periodic loop, see Fig. 2.8, showing that the locomotion on water took place at an approximately constant velocity > 2 cm s^{-1} throughout the whole experiment of 54 minutes. To show that this vapor-based Marangoni propulsion concept is general, it was demonstrated that it works also on oil, where pentane was used as the volatile fuel (at 20°C $\sigma_{\text{paraffin oil}}$ = 32.9 mN m^{-1}, σ_{pentane} = 15.8 mN m^{-1})

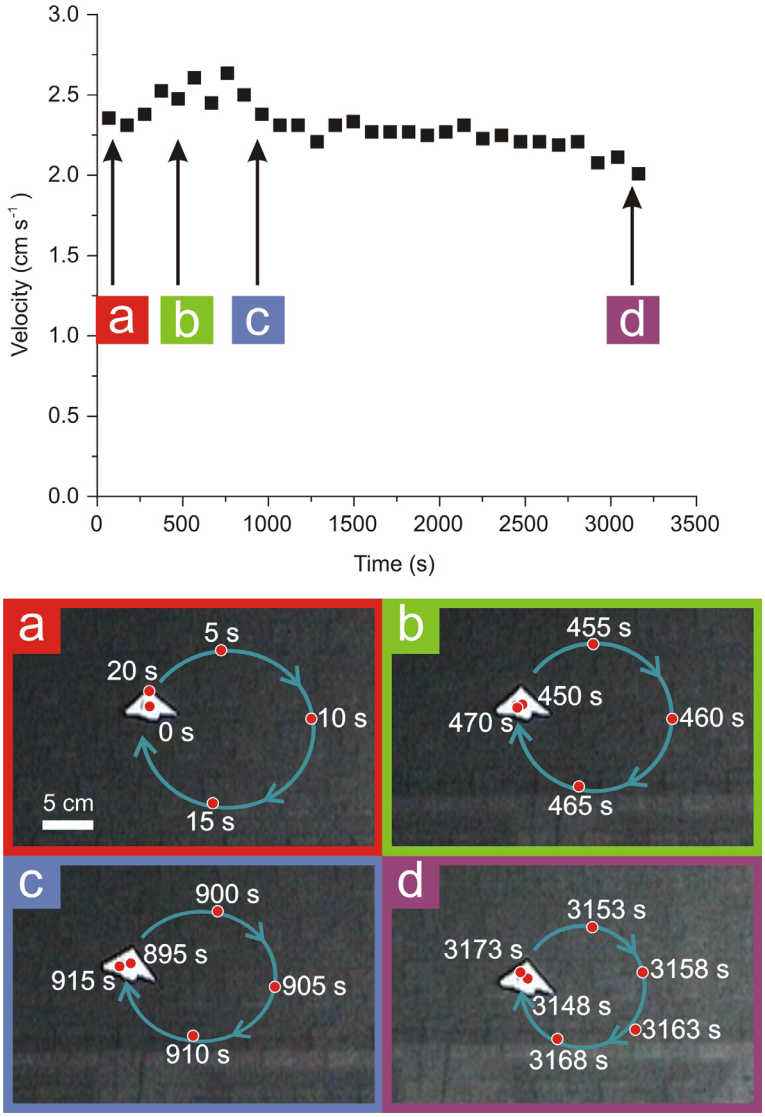

Figure 2.8 Steady-velocity locomotion on water based on nanostructured superhydrophobic and superoleophobic NFC aerogel membranes with on-board ethanol as fuel. The vessel is designed to travel along circular trajectories at the free water surface to allow facile monitoring of the velocity. The graph shows the velocity as function of time. Each data point corresponds to the average velocity for travelling five circular trajectories. Snapshots of the video show the trajectories of the aerogel vessel (time intervals 0-20 s, 450-470 s, 895-915 s and 3148-3173 s). The red spots in a-d are the positions of the vessel.

Tunability of the velocity was demonstrated by changing the type of fuel (see Fig. 2.9). We selected a series of alcohols with increasing chain length, ranging from methanol to *n*-heptanol, and we observed that the velocity of the aerogel vessel decreases accordingly. The decreased vapor pressure

leads to less alcohol to modify the water surface and correspondingly lower surface tension gradient leads to decreased velocity.

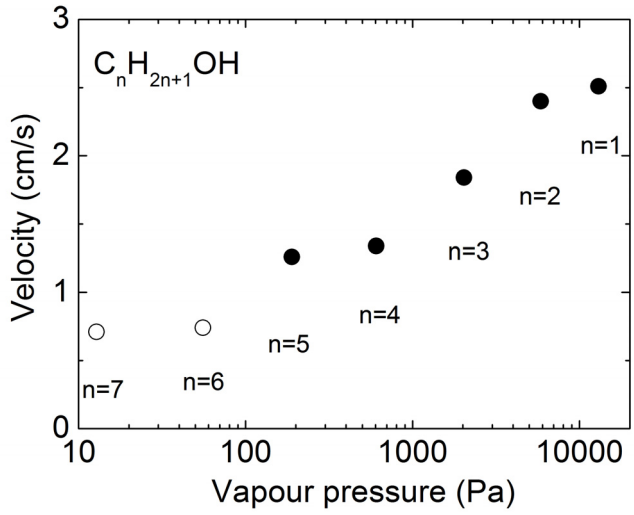

Figure 2.9 Tuning the velocity of aerogel locomotion on water by fuel vapors of linear alcohols with different vapor pressure (from methanol to *n*-heptanol). The vapor pressure at 20 °C are determined from the Antoine equation using parameters obtained from NIST Chemistry WebBook (the open circles are approximate values of vapor pressure, calculated by extrapolating the Antoine equation beyond the temperature range of its applicability).

Next, it was demonstrated that vapor-driven Marangoni propulsion worked also for objects travelling on oil, where pentane was used as the volatile fuel (at 20°C $\sigma_{paraffin\ oil}$ = 32.9 mN m^{-1}, $\sigma_{pentane}$ = 15.8 mN m^{-1}), see Fig. 2.10. Although the surface tension gradient (and consequently the driving force) is significantly smaller than for the water-ethanol system, it shows that this vapor-based Marangoni propulsion concept is general.

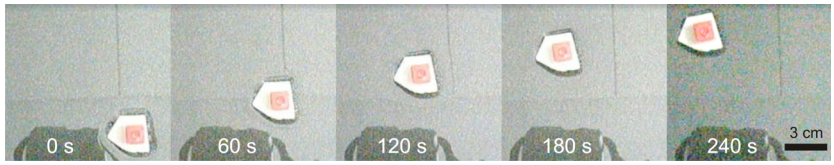

Figure 2.10 Video snapshots of the aerogel vessel locomoting on paraffin oil using pentane vapor as the propelling agent.

Inspired by locomotion and floatation of insects on water, we introduce simple concepts of autonomous devices for locomotion, floatation, and load carrying of miniaturized objects on water and oil. In this work, we use fluorinated NFC aerogels as membranes to provide gas-permeability and liquid-impermeability, due to their superhydrophobic and superoleophobic properties and gas permeability. The simple selectivity between gases and liquids could allow energy transduction from chemical energy to kinetic energy, is inspired by biological systems, where much more complex membranes with refined selectivities are ubiquitous for various energy transductions. In contrast to catalytic propulsion systems requiring floatation on a special fuel-containing solution (e.g. Pt-decorated boats floating on H_2O_2 aqueous solution) *[76, 77]*, the present locomotion concept is more general as it is valid also on pure water and oil because the object carries its own fuel. This may open ways towards new applications ranging from autonomous environmental monitoring, surveillance to chemical sensing, using fuel-driven soft devices, as the materials and processes are readily available. We expect that membrane-based energy transduction might be generalized also for other dissipative processes. The concept may open new schemes for biomimetic autonomous soft devices.

3. Damage-Resistant Non-Wetting

3.1 Background

Even though non-wetting surfaces have attractive properties *[78-81]*, their practical applications are limited by damage-resistance. In most cases, mechanical abrasion leads to damage of topographical patterns and loss of specific wetting properties. As previously stated, hierarchical rough structure is a prerequisite for constructing superhydrophobic and superoleophobic surfaces. Therefore, damage may cause lower repellency to liquids *[78]*. Damage resistant or self-healing superhydrophobicity and superoleophobicity *[9, 10]* would be interesting taken the superhydrophobicity and superoleophobicity retain after being mechanically damaged. There are three strategies for developing damage-resistant superhydrophobicity and superoleophobicity. (1) Strong films or bulk materials with superhydrophobicity and superoleophobicity that can withstand mechanical damage. Fig. 3.1 shows an example where the superoleophobic surfaces retain its superoleophobicity after abrasion with sand treatment *[9]*. However, the superoleophobic surfaces have been limited to thickness of tens of μm. (2) Self-healing materials that can recover the non-wetting properties by renewal of the exposed layer after damage or by reorientation of dangling chains. The problem with this mechanism is that it takes time to recover, and during the recovery process when the surface has low repellency, contamination may occur. (3) Preservation of both the topography and low surface energy coating, even when some surface layers are removed due to mechanical abrasion.

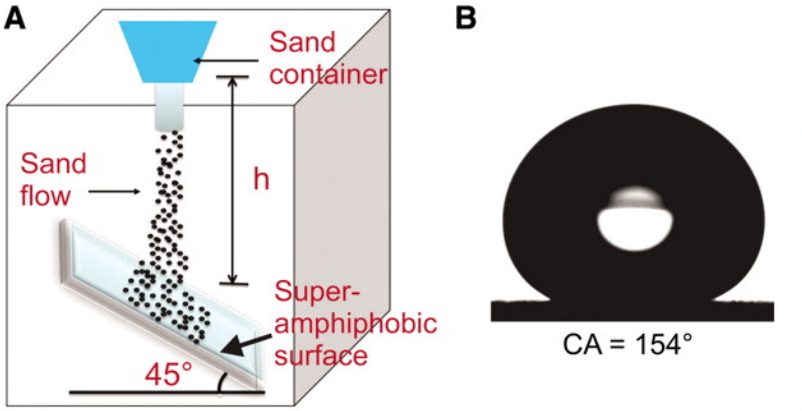

Figure 3.1 A superoleophobic coating using candle soot as a template is durable to sand flow *[9]*. (A) Schematic drawing of a sand abrasion experiment. (B) Hexadecane drop deposited on the coating after 20 g of sand abrasion from 40 cm height. The 100- to 300-μm-sized grains had a velocity of 11 km/hour just before impingement. After impingement, the drops rolled off after the substrate was tilted by 5°. (From Ref [9], Reprinted with permission from AAAS)

In this work, we present a new approach towards damage-resistant superamphiphobicity (i.e. superhydrophobicity and superoleophobicity), using aerogel materials that have a suitable nanoscale re-entrant surface topography for non-wetting to water and oil. The aerogel has fractal structures throughout the bulk, and therefore enables exposure of new re-entrant surface topographies beneath the damage zones even upon applying abrasion, thus preserving the suitable topography for non-wetting. The surfaces are made from a commercial silica aerogel that is modified by CVD with (tridecafluoro-1,1,2,2-tetrahydrooctyl) trichlorosilane (FTCS). After modification by CVD, silica aerogel has superamphiphobic properties and we further show these non-wetting properties are retained upon abrasion with sandpaper or sharp objects. More interestingly, the CA hysteresis decreases after abrasion with sand paper, and this is in contrast to most superhydrophobic or superoleophobic surfaces. The advantage of this approach is that the surface remains non-wetting during and immediately after mechanical abrasion. More importantly, this approach shows a potential new concept for removing contamination through wear. This is particularly relevant for contamination caused by particles or dusts.

3.2 Experimental and Methods

The silica aerogel was from Airglass AB, Sweden. Chemical vapor deposition was carried out on the silica aerogel using (Tridecafluoro-1,1,2,2-tetrahydrooctyl) trichlorosilane (97%, ABCR) for one week at 75 °C. The wetting properties of the modified silica aerogel surfaces were characterized by CAM 200 Optical Contact Angle Meter (KSV Instruments). In CA measurement, Milli-Q water and paraffin oil (Yliopiston Apteekki, used as received, surface tension of 32.9 mN m^{-1}) were used. In this work, advancing CA, receding CA and sliding angle were measured to determine the wetting properties of the surfaces. A drop with volume of 3 μL was applied on the surface. During measurement of advancing CA, more liquid was added at a rate of 0.5 ± 0.1 μL s^{-1} and photos were taken with 150 ± 50 ms intervals. More liquid was added to get a droplet bigger than 20 μL for receding CA measurement. Then the liquid was withdrawn at a rate of 0.5 ± 0.2 μL s^{-1} and photos were taken with 150 ± 50 ms intervals. The needle has to be close to the surface in the center of the drop, otherwise air will be taken, especially in the case of viscous liquid. Photos for drops with volume from 6.0 ± 3.0 μL were fitted by the Young-Laplace Equation. In the advancing process of a drop, the side with higher CA is more likely to advance and therefore is used as advancing CA. However, in the receding process, the side with lower CA is more likely to recede and is used as the receding CA. For measuring sliding angle, a drop with volume of 5.0 ± 2.0 μL was applied on the surface with increasing tilting angle. The sliding angle is the tilting angle when the droplet slides or rolls away from the surfaces.

JEOL JSM-7500 field emission scanning electron microscope (FE-SEM) was applied to characterize the morphology of the silica aerogel. Sputter coating with gold was done at 20 mA for 1 min before SEM characterization to avoid charging problems.

3.3 Results and Discussion

The silica aerogel shows good transparency in Fig. 3.2 a. Fig. 3.2 b and c show the SEM images of silica aerogel. It can be seen that there is hierarchical structure of platelets in μm length scale and silica spheres in nm length scale. In Fig. 3.2 b, silica aerogel shows rough structures in μm scale and this is helpful in achieving superhydrophobicity and

superoleophobicity. With higher magnification in Fig. 3.2 c, there exists a highly porous structure with pores and protrusions. Most of the pores and protrusions have size less than 1 μm and they form re-entrant structures *[8]*. Tuteja et al. discussed the importance of the re-entrant structures in obtaining superoleophobic surfaces. They came up with a new concept of spacing ratio in designing superoleophobic surfaces *[8]*. Not only the size of features but also the distance between features affects the wetting properties of surfaces. From Fig. 3.2 d, there are fractal structures of clusters of silica spheres with diameter of tens of nm. The distance between neighboring silica spheres is even shorter than the diameter of silica spheres and this is helpful in achieving superoleophobic surfaces as discussed above. In this case, mechanical effects will not damage the fractal structure in Fig. 3.2 d. This is important for retaining superhydrophobicity and superoleophobicity after mechanical damage.

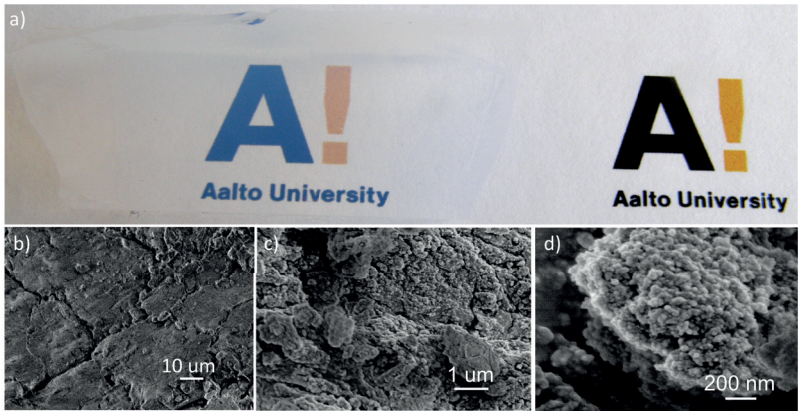

Figure 3.2 Images of silica aerogel. (a) Photo of a piece of silica aerogel with thickness of ca. 2 cm shows transparency. (b) SEM image shows hierarchical structures of silica aerogel in the scale of μm and nm (c). Silica spheres are shown with size of tens of nm in SEM image (d).

The contact angle (CA) hysteresis, that is defined as the difference between the advancing CA and receding CA, is an important parameter to characterize superhydrophobic and superoleophobic surfaces. On surfaces with low CA hysteresis, liquid droplets roll off easily with very low friction. In many cases, damage or contamination does not have much effect on the advancing CA, but it can decrease significantly the receding CA. Therefore, the CA hysteresis increases, leading to higher adhesion between surface and liquid, i.e., droplet pinning.

In this work, a silica aerogel was abraded by sandpaper, removing 660 μm of material after 100 abrasion cycles. Advancing and receding CAs are

shown in Fig. 3.3 as a function of abrasion cycles for water and paraffin oil. Advancing and receding CAs for water are 172° and 150° before abrasion, respectively, corresponding to CA hysteresis of 22°. For paraffin oil, the initial advancing and receding CAs are 168° and 130°, indicating a larger CA hysteresis. Curiously, upon applying abrasion, the advancing and receding CAs started to approach each other; in other words the CA hysteresis decreases (Fig. 3.3 A). For water, the CA hysteresis becomes eventually as small as 1° upon 100 abrasion cycles (Fig. 3.3 B) and for oil it reaches 11° (Fig. 3.3 C). The low CA hysteresis upon abrasion manifests also in reduced sliding angles. Fig. 3.3 D shows that a 5 µl paraffin oil droplet slides off easily at a small tilt angle of 10° before the abrasion. However, after the 100 cycles of abrasion, the tilt angle becomes drastically reduced to 2° (Fig. 3.3 E). This indicates that upon abrasion the surface has become highly repellent to oils and also water. These final values after exposed mechanical damage are remarkably good even in comparison with initial values in other studies. Tuteja et al. designed superoleophobic surfaces based on re-entrant structures and the CA hysteresis for hexadecane was 6° and the sliding angle 5° *[8]*. Recently, Deng et al. used candle soot as a template to achieve a superamphiphobic coating with sliding angle of 5° for olive oil *[9]*.

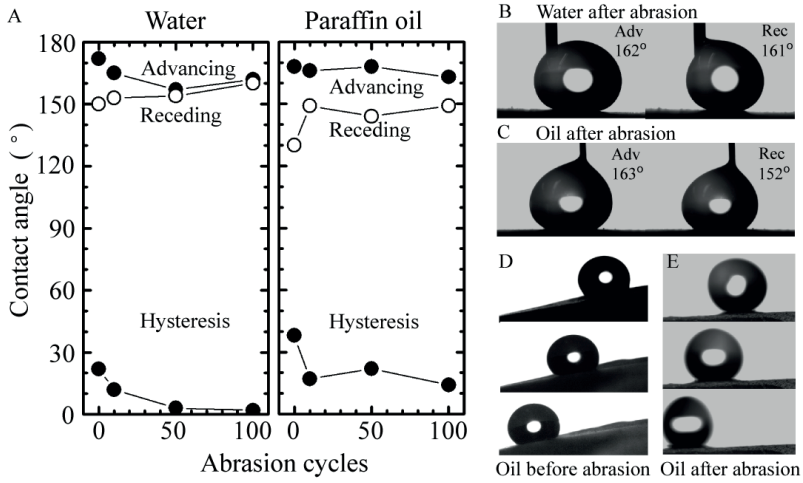

Figure 3.3 Wetting properties of the superoleophobic and superhydrophobic surface before and after abrasion with sandpaper. (A) Contact angle data vs. abrasion cycles. (B) Advancing and receding CA for water after 100 cycles of abrasion. (C) Advancing and receding CA for paraffin oil after 100 cycles of abrasion. (D) Sliding angle of 10° demonstrated for paraffin oil before abrasion (frame intervals of 0.1 s). (E) Sliding angle of 2° demonstrated for paraffin oil after 100 cycles of abrasion (frame intervals of 0.12 s).

In contrast to most superhydrophobic and superoleophobic surfaces, the liquid repellency in this work exhibits high resistance against

mechanical damage. We suggest that the fractal structure in Fig. 3.4 A is essential for preserving the topography even upon abrasion. Though it is remarkable that upon damage the newly created surface at the broken necks does not contribute to increase of the contact angle hysteresis. We expect that upon abrasion the thin necks between two silica nanospheres break, being weak links (see Fig. 3.4 C), and the bare silica surface of the aerogel skeleton becomes exposed locally at the site of the broken neck. We hypothesize that the exposed silica surface gets partially covered by the tail of the fluorosilane. Another possible mechanism is based on migration of unreacted chlorosilane from neighboring regions for the replenishment of the newly exposed area as is shown in Fig. 3.4 C. As the broken surface area is relatively small, only low number of chlorosilane molecules are sufficient to replenish the exposed areas, thereby providing healing of the coating. The increase in receding contact angle upon abrasion may be caused by the removal of defects on the aerogel surface.

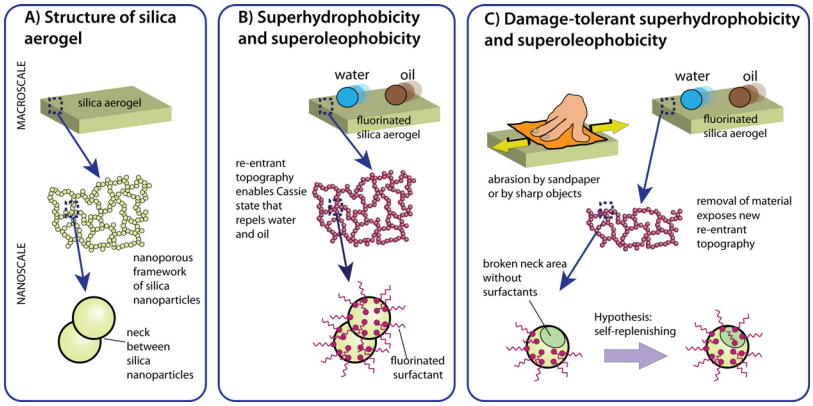

Figure 3. 4 (A) Schematic representation of silica aerogel with its fractal-like structure formed by silica nanoparticles. (B) Silica aerogel has a re-entrant surface topography that renders it superhydrophobic and superoleophobic when modified with a fluorinated surfactant. (C) Mechanical abrasion by sandpaper or sharp objects leads to removal of part of the aerogel material and rupture of the necks that bond two nanoparticles together. Despite severe damage, the newly exposed aerogel surface still has superhydrophobic and superoleophobic properties with low contact angle hysteresis and low sliding angles. At the broken neck area silanols become exposed, though we hypothesize the broken neck area gets replenished with surfactant molecules migration from neighboring regions

In summary, superhydrophobic and superoleophobic surfaces have been obtained from silica aerogel with low sliding angle for water and paraffin oil. It has to be noticed the liquid repellency remains after mechanical abrasion, what is in contrast to most superhydrophobic and superoleophobic surfaces. More interestingly, the contact angle hysteresis

decreases for water and oil after abrasion, indicating higher liquid-repellency after sand abrasion. There are two advantages of this concept. One is that it does not need time to recover the liquid-repellency after mechanical damage. This avoids possible contamination during recovery process as in the case for self-healing superhydrophobic and superoleophobic materials. The other is that contaminates of particles and dusts can be removed upon wear to keep the liquid repellency. Considering the development in strong and tough aerogels by incorporating different components, the concept shows light in practical applications of durable superhydrophobic and superoleophobic materials.

4. Tough Bulk Nanocomposites

4.1 Background

4.1.1 Development of Tough Nanocomposites

Nature has its own sophisticated way to synthesize lightweight biomaterials with extremely high toughness combining strength and stiffness. Nacre and bone are classical examples of tough biomaterials. However, they are not technologically feasible due to complexity of the biological systems. Though, they have attracted increasing scientific interests in understanding the toughening mechanisms behind them *[16, 17]* and hence designing biomimetic routes for tough materials *[14, 82-84]*. It has been found that in both nacre and bone, there are hierarchical structures incorporating inorganic and organic components, where inorganic component provides stiffness and organic component provides strength *[14, 16, 82, 84]*. Nacre comprises more than 90% of minerals, though its toughness is some three orders of magnitude higher than that of pure minerals *[20]*. In bone, there are 65% hydroxyapatite minerals and 25% collagen fibrils *[12, 13]*. Learning from nacre and bone, there are two aspects to be considered in biomimetic strategies for tough materials. One is the complex hierarchical structure to dissipate energy from short range to long range *[13, 16, 17, 20]*. The other is the well-controlled interaction between inorganic and organic components that enables proper adhesion and energy dissipation between inorganic and organic parts *[14, 17, 82, 84-89]*.

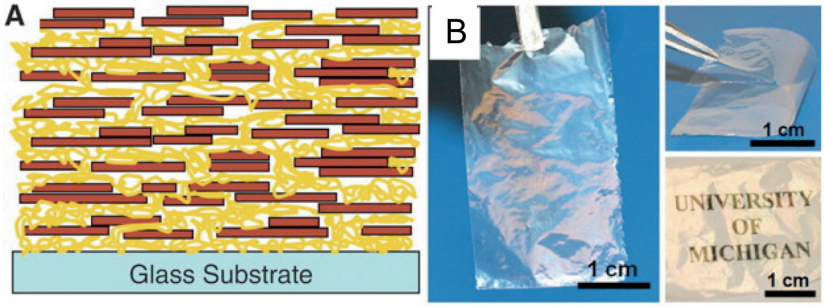

Figure 4.1 Preparation of polyvinyl alcohol/montmorillonite (PVA/MTM) layered nanocomposites by sequential depositions *[90]*. (**A**) Schematic representation of the internal architecture of the PVA/MTM nanocomposite (picture shows 8 bilayers). (**B**) Free-standing, 300-bilayer PVA/MTM composite film showing high flexibility and transparency. The lower image was taken at an angle to show diffraction colors. (Reprinted from Ref [90] with permission from AAAS)

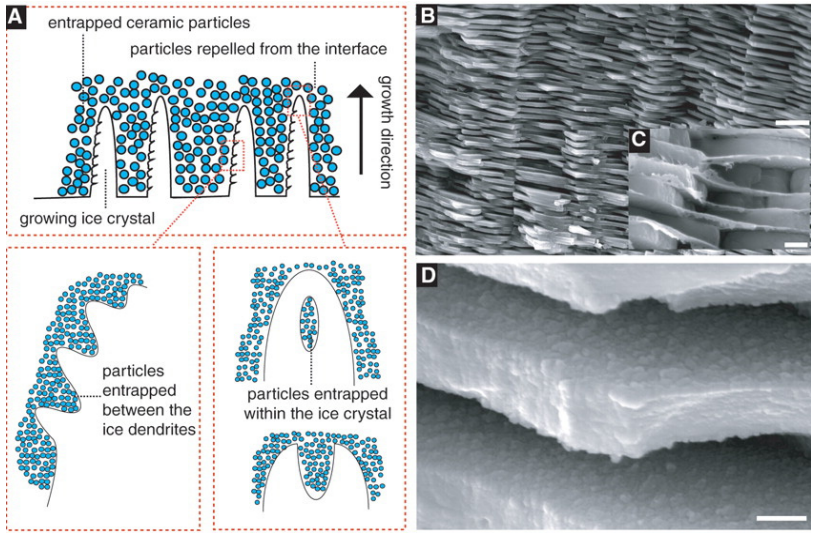

Figure 4.2 Processing principles and materials based on ice-templating and sintering towards nacre-mimetic materials *[82]*. Upon freezing of the ceramic aqueous slurry, the growing ice crystals expel the ceramic particles, creating a lamellar microstructure oriented in a direction parallel to the movement of the freezing front (A). For highly concentrated slurries, the interaction between particles becomes critical: A small fraction of particles are entrapped within the ice crystals by tip-splitting and subsequent healing (A), leading to the formation of inorganic bridges between adjacent walls. Dense composites are obtained by infiltrating the porous lamellar ceramic with a second phase (e.g., a polymer or a liquid metal). Natural nacre has a brick-mortar-bridges microstructure where inorganic calcium carbonate layers are held together by organic protein "glue" (B and C); the roughness of the inorganic walls (D) is a key contributor to the final mechanical properties of nacre. Scale bars indicate (B) 5 μm, (C) 0.5 μm, (D) 0.3 μm. (Reprinted from Ref [82] with permission from AAAS)

Even though thorough understanding of the toughing mechanisms of biomatter is a considerable scientific challenge as such, there has been promising development in material science mimicking nacre and bone. Layer-by-layer deposition (LBL) *[83, 90, 91]* and spin coating *[84]* are classical strategies to achieve films in mimicking layered hierarchical structures of nacre. Kotov et al. prepared transparent freestanding films from polyvinyl alcohol (PVA) and MTM (Fig. 4.1), showing attractive mechanical properties *[83]*. Directional freezing *[14, 82]* as shown in Fig. 4.2, typically combines sintering and allows tough bulk materials. By well-controlled freezing kinetics in Fig. 4.2 A, layered microstructure with order (Fig. 4.2 B-D) can be obtained. Although some materials having remarkably high mechanical properties are made from those methods, the sequential LBL and spin coating are time-consuming and directional freezing combining sintering is energy-consuming. A fast, economic and green

strategy of filtration has been introduced for producing large-area and lightweight composites (Fig 4.3) with high stiffness and strength in films *[85]*. In this work, we will show a one-step process of centrifugation to prepare tough bulk materials to integrate NFC and MTM.

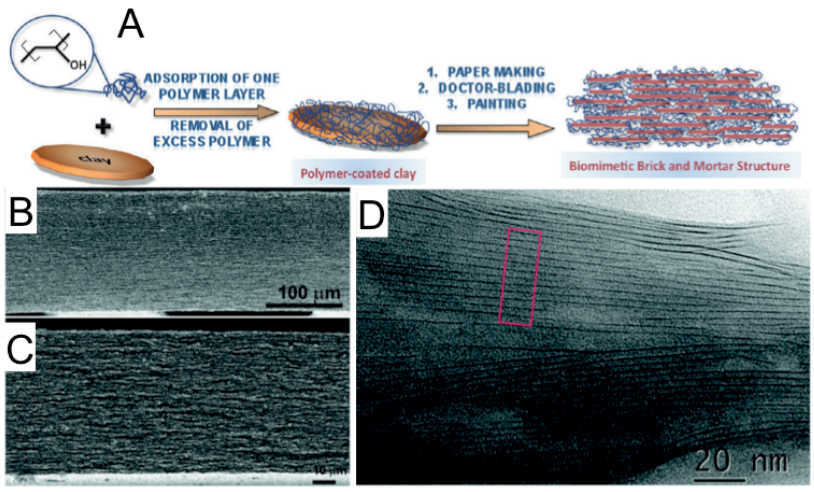

Figure 4.3 (A) A scheme of the preparation method of layered PVA/MTM nacre-mimetic composites obtained via one-step self-assembly, based on PVA deposition on MTM platelets and subsequent self-assembly upon water removal. (B+C) show SEM images of films of thicknesses of 0.17 and 0.063, mm, demonstrating that even thick films can be prepared and the film thickness can be tuned. The high resolution TEM image in (D) confirms the well-spaced layered structure. (Reprinted from Ref [85] with permission from Copyright © 2010, American Chemical Society)

4.1.2 Nanocomposites from Nanofibrillated Cellulose

NFC is chosen to integrate MTM because of its good biocompatibility, high mechanical properties and sustainable availability. It is cleaved from wood in the form of hydrogel and the nanofibers have diameter in the range of tens of nm and length of several µm. Recently, hybrid nanopaper has been prepared by combining NFC and MTM by filtration *[32]*. However, there was no significant toughing or reinforcement in the composite, which is probably due to poor interaction between NFC and MTM. Strong composite films were made from TEMPO-cellulose combining MTM *[92]*. Another interesting nanocomposite was made from NFC and graphene by adding proteins that allow exfoliation of graphene and ensure good interaction of NFC and graphene (Fig. 4.4) *[93]*. Besides strong composites *[94, 96]*, functional materials based on nanocellulose such as magnetic materials

[33], photoswitchable superabsorbents and recyclable oil absorbents *[81, 95]* have been developed in recent years.

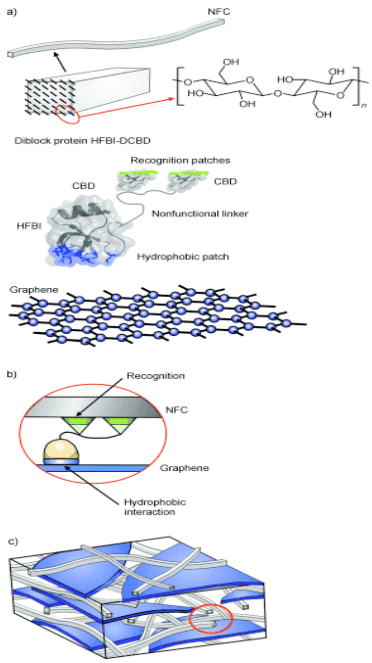

Figure 4.4 A schematic presentation of the structure of a composite. *[93]* (a) At the molecular level there are two functional blocks of the fusion protein hydrophobin and two cellulose binding domains (HFBI-DCBD) and its target surfaces, that is, graphene and nanofibrillated cellulose (NFC). The amphiphilic hydrophobin (HFBI) attaches to graphene and the cellulose-binding domains (CBDs) to NFC. (b) Diblock binding protein. The fusion protein is able to assemble at the interface between cellulose and graphene. For enhanced and balanced binding, two cellulose-binding domains are located in tandem positions. (c) Graphene/NFC/diblock binding protein assembly. At the microscopic level the composite has a layered structure wherein graphene flakes are interlocked by the NFC fibrils. (Reprinted from Ref [93], with permission from John Wiley & Sons)

In this work, a bulk nanocomposite material was obtained from forced assembly of NFC and MTM using a particularly simple process by centrifugation. NFC with cationic surface charge is used to strengthen the interaction with anionic MTM without using additional gluing components. The composite with MTM/C-NFC of 63/37 w/w has high compressive strain to failure of 37% with distinct plastic deformation behaviour, high work to fracture of 23.1 MJ/m^3, and relatively high compression strength of 76 MPa. Considering the simple preparation method and bio-based origin of NFC, we expect that the present tough bulk nanocomposites in compression have potential in applications for sustainable and environmentally friendly materials in construction and transportation.

4.2 Experimental and Methods

Cationic NFC (C-NFC) was supplied by Innventia AB (Sweden). It is semi-transparent hydrogel with *N*-(2,3 epoxypropyl)trimethylammonium functionalities on the surface. The degree of substitution is 0.089, i.e. the total charge is of 509.2 microeq./g. Its aqueous suspension of concentration of 0.023 wt-% was used in this work. NFC fibrils have diameter in the range of 5-10 nm, their length is in the range of micrometer, and they form entangled networks. MTM is an aluminosilicate clay named Bentonite from Sigma-Aldrich (CAS 1302-78-9 from Batch 067K0043). The platelets have lateral dimension up to 1 μm and MTM nanoplatelets are known to have thickness of ca. 1 nm. A 2 wt-% MTM suspension in water was prepared and mixed by magnetic stirring at 400 rpm for 24 h. C-NFC hydrogel was added to MTM suspension drop by drop to obtain MTM/C-NFC ratio of 91/9, 81/19, 63/37, and 50/50 w/w. The colloidal mixture of MTM and NFC was then mixed by Ultraturrax mixer at 10,000 rpm for 1-2 min. The suspension with MTM and NFC was transferred to a 5 mL centrifugation tube. Centrifugation was done at 4000 rpm for 5 min. In order to obtain sufficiently thick 3D samples, further amount of suspension of the mixture was added to the centrifugation tube after removing water on top. This was repeated 2 or 3 times. Thereafter the samples were dried at 60 °C for 2 days.

SEM images were taken using Hitachi S 4800 and JEOL (JSM 7500 A) field emission microscope. A thin layer of Au was sputtered onto the samples before imaging. TEM images were obtained by a JEOL JEM-3200FSC cryo-TEM. Ultrathin sections were microtomed using a LEICA 125 Ultracut. Mechanical tests were carried out by Instron 5843 with 1 kN load cells using strain rate of 1 mm/min. At least 5 samples were tested in compression for each composition. The variations are shown in Table 4.1. The average results in the table were based on at least 3 samples. The composition MTM/C-NFC of 63/37 w/w was characterized in more depth due to its close to optimal properties. During the cyclic compression test, it was compressed 5 times with setting strain of 5%. Humidity during mechanical was 20-31 % as average from the measurement room. The density of the sample with composition of MTM/C-NFC of 63/37 w/w was 2.17 g/cm^3.

4.3 Results and Discussion

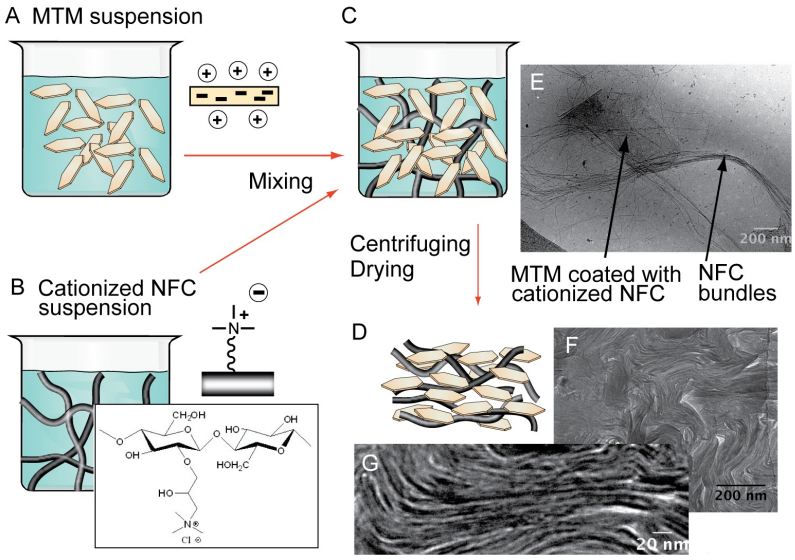

Figure 4.5 Scheme of the process to prepare tough biocomposites under compression. A) 2 wt-% suspension of MTM. B) 0.23 wt-% hydrogel of C-NFC with surface groups of N-(2,3 epoxypropyl)trimethylammonium. C) The aqueous MTM and C-NFC suspensions mixed. D) Composite material after forced packing by centrifugation and drying. E) Cryo-TEM image for the case C. F) Cross sectional TEM image of D showing local self-assembled domains. G) Lower magnification TEM shows that the domains do not have overall alignments.

Fig. 4.5 shows a scheme for the preparation. Firstly, C-NFC and MTM were separately dispersed in water, which leads to essentially clear suspensions. Thereafter the two dispersions were mixed at relative weight fractions MTM/C-NFC 91/9, 81/19, 63/37, and 50/50 w/w. We selected high weight fraction of the inorganic component because biomimetic design principles suggest high levels of reinforcements. The resulting mixtures showed increased turbidity (Fig. 4.6 B) due to the formation of large colloidal complexes as the oppositely charged C-NFC can bridge several MTM nanoplatelets to form ionically bound networks. Fig. 4.5 E shows a MTM platelet having a lateral dimension of ca. 300 nm, binding NFC fibrils where two NFC bundles are resolved. Typically, floc-like aggregates in preparation suspensions would be regarded to be detrimental to achieve well-defined self-assemblies and long-range order in the final compositions due to packing frustrations caused by aggregates. But interestingly, upon forced packing by centrifugation followed by drying, one obtains local self-assemblies (Fig. 4.5 G). Even if Fig. 4.5 G shows domains of aligned self-assemblies, the periodicity is not exactly defined, being in the range of 5-10

nm. NFC has a diameter in the same range as deduced from the cryo-TEM image in Fig. 4.5 E. Note that a single exfoliated MTM has a thickness of ca. 1 nm. A loose intercalation of the C-NFC can lead to nanovoids between the nanoplatelets and defect domains are observed between the self-assembled domains. Fig. 4.5 F shows the structure at larger length scale: in the range of tens of nm, layered domains are observed, while in the range of hundreds nm, the structure becomes isotropic, as there is no coordinated alignment between the domains. Note that the dense set of microvoids and defects may play important role for the pronounced observed toughness, as it has been shown that a dense set of defects can provide deflected pathways for crack propagation in model system.

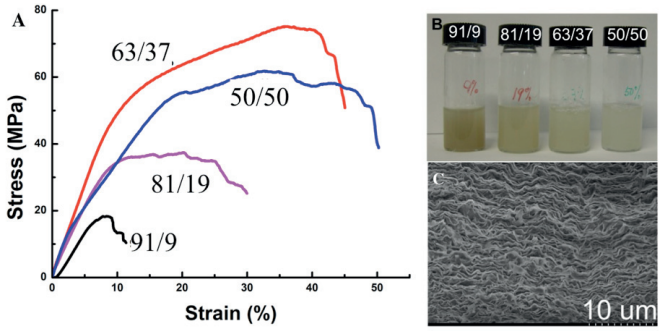

Figure 4.6 A) Compressive stress-strain curves for the MTM/C-NFC of 91/9, 81/19, 63/37, 50/50 w/w. Except for the first one, all of the compositions show distinct plastic deformation. The composition 63/37 w/w shows the best performance and is described more closely. B) The aqueous C-NFC and MTM suspensions become turbid upon mixing, indicating aggregate formation. C) SEM image of composite MTM/C-NFC of 63/37 w/w, indicating “wavyness” of the assembly, which may also promote toughness.

Compressive stress-strain measurements are shown in Fig. 4.6 A. The composition with MTM/C-NFC of 91/9 w/w shows relatively low strain to failure and strength compared to other composites in this work. The material eventually demonstrates catastrophic failure in a brittle manner as the material totally disintegrates into small pieces under compression as shown in Fig. 4.7 C. This is because the composite cannot sufficiently dissipate energy at such a high content of MTM. However, when more C-NFC is added to the composite, strain to failure, stiffness and strength are increased substantially in a synergistic manner. For the sample with MTM/C-NFC of 81/19 w/w, the stress-strain curve shows a plateau for strains > 10% indicating onset of plastic deformation. The best mechanical properties were observed for MTM/C-NFC with 63/37 w/w where the

strain is very high; close to 37% and the strength and modulus are 75.6 MPa and 512 MPa (shown in Table 4.1), respectively. The area below the stress-strain curve, i.e. work to fracture, gives a qualitative measure of the toughness, and in the present case, it is as high as 23.1 MJ/m^3. Finally, further increasing the weight fraction of C-NFC for MTM/C-NFC 50/50 w/w leads to decreased mechanical properties, indicating the composition 63/37 w/w is close to optimal.

Table 4.1 Summary of the mechanical properties of various nanocomposites with different compositions.

Composite	Compressive Strength (MPa)	Modulus (MPa)	Work to Fracture (MJ /m^3)
91/9 w/w	22.3±4.8	339±25	2.49±0.7
81/19 w/w	38.7±12.5	454±35	12.3±0.1
63/37 w/w	75.6±1.6	512±94	23.1±5.4
50/50 w/w	64.2±7.7	379±40	22.7±2.0

In the composites, clay provides stiffness while cellulose acts as viscoelastic glue to dissipate energy and therefore provides strength. Strength and stiffness is usually a compromise to each other, which makes design of tough materials more difficult. When cellulose is less than optimal, energy accumulated during deformation cannot dissipate well and will lead to catastrophic failure as is shown in Fig. 4.7 C. When cellulose is more than optimal, there will be decrease in stiffness as in the case with 50/50 MTM/C-NFC w/w.

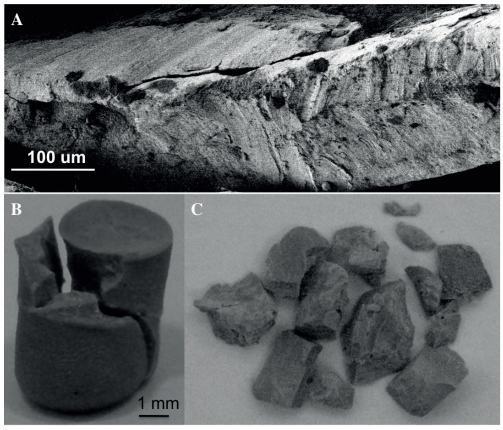

Figure 4.7 Examples of fractures. A) Cross sectional SEM image of cracks from the composite with MTM/C-NFC of 63/37 w/w showing rough crack surfaces. B) MTM/C-NFC 63/37 w/w after compression failure, showing deflected crack path. C) Photo of pieces from composite with MTM/C-NFC of 91/9 w/w after compression failure, indicating brittleness.

Another evidence of the toughness is given upon studying the fracture of the sample with C-NFC/MTM of 63/37 w/w, see Fig. 4.7 A and B, where the crack propagates in a deflected and tortuous way. Finding molecular and structural level origins for the high toughness is a challenging task, probably requiring multi-scale modeling in combination with extensive fracture analysis with in-situ observations *[19]*. At this point we can only give hypotheses for the high toughness. We expect that the ionic interaction between the MTM and C-NFC are relevant, akin to the ionic interactions between minerals and collagen in bone *[96]*. The forced assembly by centrifugation leads to packing imperfections, defects and nanovoids (Fig. 4.7). This combines with the “wavy” structure formed by C-NFCs, and MTM have favorable effects on the extent of plastic deformation in compression.

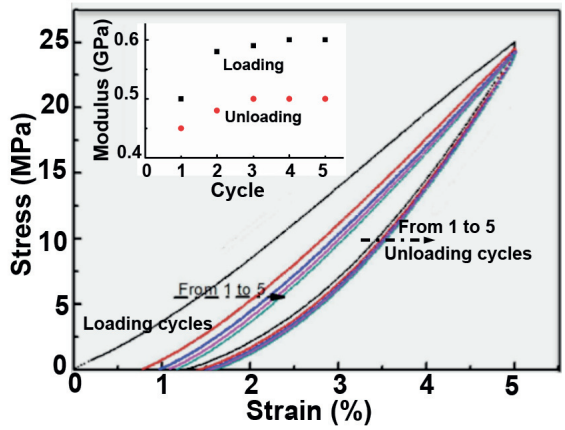

Figure 4.8 Cyclic compressive properties of the composite with MTM/C-NFC of 63/37 w/w in 5 cycles. Inset shows the development of the modulus under consecutive loading and unloading.

Cyclic compression results for the synergistic composition of 63/37 w/w are shown in Fig. 4.8. It demonstrates the hysteresis during loading and re-loading, which is a manifestation of the energy dissipation. A relatively low strain of 5% is applied, which is much less than the maximum strain of nearly an order of magnitude larger because elasticity is more interesting in this area. It can be seen that after unloading in Cycle 1, there was 0.8% permanent residual strain in the material. The stiffness does not change much in different cycles of loading, neither in the cycles of unloading. This suggests that there are neither significant cracks in MTM platelets during reloading process, nor significant breaks of bonds between MTM and NFC. *[20]*

In summary, in this work, a facile one-step route for a bulk 3D composite material with particularly high strain to failure, distinct plastic deformation and high toughness in combination with high strength under compression was demonstrated from cationic cellulose nanofibrils and anionic montmorillonite using forced assembly by centrifugation. This is encouraging, since the realization of load-bearing tough structural nanocomposites in bulk form is an important challenge in materials science. The optimal composition MTM/C-NFC of 63/37 w/w showed strain to failure of 37%, strength of 76 MPa, and high work to fracture of 23.1 MJ/m^3 under compression. Considering the simple preparation methods, potentially low cost, and bio-based origin of NFC, the composites have potentials for applications in construction and transportation.

5. Conclusions and Outlook

To conclude, bio-inspired materials for cargos, self-propulsion, self-cleaning and toughness have been achieved. Firstly, superhydrophobic and superoleophobic aerogels from nanocellulose were prepared for cargos. They allow efficient floating of miniaturized rafts on water and oil due to surface tension. Due to Marangoni effect, organic vapors can modify the surface tension underneath the superoleophobic aerogel and therefore drives continuous propulsion. This allows transduction of chemical energy into motility. This could open doors for new generation of autonomous soft machines.

Furthermore, preservation of superhydrophobicity and superoleophobicity upon wear is demonstrated from silica aerogel by chemical vapor deposition. Interestingly, the contact angle hysteresis decreases after abrasion with sand paper, which is in contrast to most superhydrophobic and superoleophobic surfaces. There are two advantages of this concept. One is that it retain self-cleaning immediately after the mechanical damage. The other is that contaminates such as particles and dusts are removed by wear. Taken the recent progress towards robust aerogels, we foresee that the concept open routes for various applications.

Finally, a tough composite is achieved from nanofibrillated cellulose and nanoclay by a simple centrifugation method. The work to fracture in compression is even higher than that of bone and nacre due to high strain to failure. This is remarkable, taken the simple processes. We hope that this shows light in designing and processing cellular tough materials.

6. References

[1] **M. Liu, Y. Zheng, J. Zhai, L. Jiang, *Acc. Chem. Res.* 2010, *43*, 368.**

[2] **A. Marmur, *Langmuir* 2008, *24*, 7573.**

[3] **D. Quéré, *Annu. Rev. Mater. Res.* 2008, *38*, 71.**

[4] **F. Xia, L. Jiang, *Adv. Mater.* 2008, *20*, 2842.**

[5] **X. Gao, L. Jiang, *Nature* 2004, *432*, 36.**

[6] **X. Zhang, F. Shi, J. Niu, Y. Jiang, Z. Wang, *J. Mater. Chem.* 2008, *18*, 621.**

[7] **K. S. Liu, L. Jiang, *Nano Today* 2011, *6*, 155.**

[8] **A. Tuteja, W. Choi, M. Ma, J. M. Mabry, S. A. Mazzella, G. C. Rutledge, G. H. McKinley, R. E. Cohen, *Science* 2007, *318*, 1618.**

[9] **X. Deng, L. Mammen, H. J. Butt, D. Vollmer, *Science* 2012, *335*, 67.**

[10] **Y. Li, L. Li, J. Q. Sun, *Angew. Chem. Int. Ed.* 2010, *49*, 6129.**

[11] **H. X. Wang, Y. H. Xue, J. Ding, L. F. Feng, X. G. Wang, T. Lin, *Angew. Chem. Int. Ed.* 2011, *50*, 11433.**

[12] **M. A. Meyers, P.-Y. Chen, A. Y.-M. Lin, Y. Seki, *Prog. Mater. Sci.* 2008, *53*, 1.**

[13] **M. E. Launey, R. O. Ritchie, *Adv. Mater.* 2009, *21*, 2103.**

[14] **E. Munch, M. E. Launey, D. H. Alsem, E. Saiz, A. P. Tomsia, R. O. Ritchie, *Science* 2008, *322*, 1516.**

[15] **P. Fratzl, R. Weinkamer, *Prog. Mater. Sci.* 2007, *52*, 1263.**

[16] **H. Peterlik, P. Roschger, K. Klaushofer, P. Fratzl, *Nat. Mater.* 2006, *5*, 52.**

[17] **M. E. Launey, M. J. Buehler, R. O. Ritchie, *Annu. Rev. Mater. Res.* 2010, *40*, 25.**

[18] **M. J. Buehler, *Proc. Natl. Acad. Sci. U. S. A.* 2006, *103*, 12285.**

[19] **D. Sen, M. J. Buehler, *Sci. Rep.* 2011, *1*.**

[20] **R. Z. Wang, H. S. Gupta, *Annu. Rev. Mater. Res.* 2011, *41*, 41.**

[21] **T. Zimmerman, E. Pöhler, T. Geiger, *Adv. Eng. Mater.* 2004, *6*, 754.**

[22] **M. Pääkkö, M. Ankerfors, H. Kosonen, A. Nykänen, S. Ahola, M. Österberg, J. Ruokolainen, J. Laine, P. T. Larsson, O. Ikkala, T. Lindström, *Biomacromolecules* 2007, *8*, 1934.**

[23] **M. Pääkkö, J. Vapaavuori, R. Silvennoinen, H. Kosonen, M. Ankerfors, T. Lindström, L. A. Berglund, O. Ikkala, *Soft Matter* 2008, *4*, 2492.**

[24] **S. J. Eichhorn, A. Dufresne, M. Aranguren, N. E. Marcovich, J. R. Capadona, S. J. Rowan, C. Weder, W. Thielemans, M. Roman, S. Renneckar,**

W. Gindl, S. Veigel, J. Keckes, H. Yano, K. Abe, M. Nogi, A. N. Nakagaito, A. Mangalam, J. Simonsen, A. S. Benight, A. Bismarck, L. A. Berglund, T. Peijs, *J. Mater. Sci.* 2010, *45*, 1.

[25] D. Klemm, F. Kramer, S. Moritz, T. Lindstrom, M. Ankerfors, D. Gray, A. Dorris, *Angew. Chem. Int. Ed.* 2011, *50*, 5438.

[26] Y. Habibi, L. A. Lucia, O. J. Rojas, *Chem. Rev.* 2010, *110*, 3479.

[27] H. Sehaqui, A. D. Liu, Q. Zhou, L. A. Berglund, *Biomacromolecules* 2010, *11*, 2195.

[28] J. R. Capadona, K. Shanmuganathan, D. J. Tyler, S. J. Rowan, C. Weder, *Science* 2008, *319*, 1370.

[29] M. Henriksson, G. Henriksson, L. A. Berglund, T. Lindström, *J. Eur. Polym.* 2007, *43*, 3434.

[30] H. Yano, J. Sugiyama, A. N. Nakagaito, M. Nogi, T. Matsuura, M. Hikita, K. Handa, *Adv. Mater.* 2005, *17*, 153.

[31] T. Saito, S. Kimura, Y. Nishiyama, A. Isogai, *Biomacromolecules* 2007, *8*, 2485.

[32] A. D. Liu, A. Walther, O. Ikkala, L. Belova, L. A. Berglund, *Biomacromolecules* 2011, *12*, 633.

[33] R. T. Olsson, M. A. S. A. Samir, G. Salazar-Alvarez, L. Belova, V. Strom, L. A. Berglund, O. Ikkala, J. Nogues, U. W. Gedde, *Nat. Nanotech.* 2010, *5*, 584.

[34] T. T. T. Ho, Y. S. Ko, T. Zimmermann, T. Geiger, W. Caseri, *J. Mater. Sci.* 2012, *47*, 4370.

[35] I. Burgert, M. Eder, K. Fruhmann, J. Keckes, P. Fratzl, S. Stanzl-Tschegg, *Holzforschung* 2005, *59*, 354.

[36] S. S. Kistler, *Nature* 1931, *127*, 741.

[37] R. Fu, B. Zheng, J. Liu, M. S. Dresselhaus, G. Dresselhaus, J. H. Satcher, T. F. Baumann, *Adv. Funct. Mater.* 2003, *13*, 558.

[38] R. C. Weatherwax, D. F. Caulfield, *Tappi* 1971, *54*, 985.

[39] R. W. Pekala, *J. Mater. Sci.* 1989, *24*, 3221.

[40] R. W. Pekala, C. T. Alviso, J. D. LeMay, *J. Non-Cryst. Solids* 1990, *125*, 67.

[41] R. W. Pekala, D. W. Schaefer, *Macromolecules* 1993, *26*, 5487.

[42] H. Tamon, H. Ishizaka, M. Mikami, M. Okazaki, *Carbon* 1997, *35*, 791.

[43] H. Tamon, H. Ishizaka, T. Yamamoto, T. Suzuki, *Carbon* 1999, *37*, 2049.

[44] C. Tan, B. M. Fung, J. K. Newman, C. Vu, *Adv. Mater.* 2001, *13*, 644.

[45] H. Jin, Y. Nishiyama, M. Wada, S. Kuga, *Colloids Surf. A* 2004, *240*, 63.

[46] F. Fischer, A. Rigacci, R. Pirard, S. Berthon-Fabry, P. Achard, *Polymer* 2006, *47*, 7636.

[47] M. D. Gawryla, L. Liu, J. C. Grunlan, D. A. Schiraldi, *Macromol. Rapid Commun.* 2009, *30*, 1669.

[48] F. Liebner, E. Haimer, M. Wendland, M.-A. Neouze, K. Schlufter, P. Miethe, T. Heinze, A. Potthast, T. Rosenau, *Macromol. Biosci. 10*, 349.

[49] L. Heath, W. Thielemans, *Green Chem.* 2010, *12*, 1448.

[50] H. Jin, M. Pääkkö, H. Pynnönen, J. Paltakari, A. Marmur, O. Ikkala, R. H. A. Ras, *Langmuir* 2011, *27*, 1930.

[51] D. Zhang, L. Shi, J. Fang, K. Dai, X. Li, *Mater. Chem. Phys.* 2006, *97*, 415.

[52] M. B. Bryning, D. E. Milkie, M. F. Islam, L. A. Hough, J. M. Kikkawa, A. G. Yodh, *Adv. Mater.* 2007, *19*, 661.

[53] S. J. Eichhorn, A. Dufresne, M. Aranguren, N. E. Marcovich, J. R. Capadona, S. J. Rowan, C. Weder, W. Thielemans, M. Roman, S. Renneckar, W. Gindl, S. Veigel, J. Keckes, H. Yano, K. Abe, M. Nogi, A. N. Nakagaito, A. Mangalam, J. Simonsen, A. S. Benight, A. Bismarck, L. A. Berglund, T. Peijs, *J. Mater. Sci.* 2010, *45*, 1.

[54] A. J. Svagan, M. A. S. Azizi Samir, L. A. Berglund, *Adv. Mater.* 2008, *20*, 1263.

[55] J. Zou, J. Liu, A. S. Karakoti, A. Kumar, D. Joung, Q. Li, S. I. Khondaker, S. Seal, L. Zhai, *ACS Nano* 2010, *4*, 7293.

[56] X. Gui, J. Wei, K. Wang, A. Cao, H. Zhu, Y. Jia, Q. Shu, D. Wu, *Adv. Mater.* 2010, *22*, 617.

[57] J. Cai, S. Liu, J. Feng, S. Kimura, M. Wada, S. Kuga, L. Zhang, *Angew. Chem. Int. Ed.* 2012, *51*, 2076

[58] K. H. Kim, Y. Oh, M. F. Islam, *Nat. Nanotech.* 2012, 7, 562

[59] K. H. Kim, M. Vural, M. F. Islam, *Adv. Mater.* 2011, *23*, 2865.

[60] M. Kettunen, R. J. Silvennoinen, N. Houbenov, A. Nykänen, J. Ruokolainen, J. Sainio, V. Pore , M. Kemell, M. Ankerfors, T. Lindström, M. Ritala , R. A. H. Ras , O. Ikkala, *Adv. Funct. Mater.* 2011, *21*, 510.

[61] X. Gui, A. Cao, J. Wei, H. Li, Y. Jia, Z. Li, L. Fan, K. Wang, H. Zhu, D. Wu, *ACS Nano* 2010, *4*, 2320.

[62] R. T. Olsson, M. A. S. Azizi Samir, G. Salazar-Alvarez, L. Belova, V. Ström, L. A. Berglund, O. Ikkala, J. Nogués, U. W. Gedde, *Nat. Nanotech.* 2010, *5*, 584.

[63] J. T. Korhonen, P. Hiekkataipale, J. Malm, M. Karppinen, O. Ikkala, R. H. A. Ras, *ACS Nano* 2011, *5*, 1967.

[64] J. T. Korhonen, M. Kettunen, R. H. A. Ras, O. Ikkala, *ACS Appl. Mater. Interfaces.* 2011, *3*, 1813.

[65] L. Bocquet, J. L. Barrat, *Soft Matter.* 2007, *3*, 685.

[66] **L. Joly, T. Biben, *Soft Matter* 2009, *5*, 2549.**

[67] **C. H. Choi, C. J. Kim, *Phys. Rev. Lett.* 2006, *96*, 066001.**

[68] **B. Bhushan, *Philos. Trans. R. Soc. Ser. A.* 2009, *367*, 1445.**

[69] **T. S. Wong, S. H. Kang, S. K. Y. Tang, E. J. Smythe, B. D. Hatton, A. Grinthal, J. Aizenberg, *Nature* 2011, *477*, 443.**

[70] **J. W. M. Bush, D. L. Hu, *Annu. Rev. Fluid Mech.* 2006, *38*, 339.**

[71] **A. Marmur, R. H. A. Ras, *Soft Matter* 2011, *7*, 7382.**

[72] **D. L. Hu, J. W. M. Bush, *Nature* 2005, *437*, 733.**

[73] **D. L. Hu, J. W. M. Bush, *J. Fluid Mech.* 2010, *644*, 5.**

[74] **H. Schildknecht, *Angew. Chem. Int. Ed.* 1976, *15*, 214.**

[75] **H. Jin, A. Marmur, O. Ikkala, R. H. A. Ras, *Chem. Sci.* 2012, 3, 2526**

[76] **R. F. Ismagilov, A. Schwartz, N. Bowden, G. M. Whitesides, *Angew. Chem. Int. Ed.* 2002, *41*, 652.**

[77] **W. F. Paxton, S. Sundararajan, T. E. Mallouk, A. Sen, *Angew. Chem. Int. Ed.* 2006, *45*, 5420.**

[78] **T. Verho, C. Bower, P. Andrew, S. Franssila, O. Ikkala, R. H. A. Ras, *Adv. Mater.* 2011, *23*, 673.**

[79] **H. Mertaniemi, A. Laukkanen, J. E. Teirfolk, O. Ikkala, R. H. A. Ras, *RSC Adv.* 2012, *2*, 2882.**

[80] **X. L. Tian, Y. Chen, Y. M. Zheng, H. Bai, L. Jiang, *Adv. Mater.* 2011, *23*, 5486.**

[81] **J. T. Korhonen, M. Kettunen, R. H. A. Ras, O. Ikkala, *ACS Appl. Mater. Interfaces.* 2011, *3*, 1813.**

[82] **S. Deville, E. Saiz, R. K. Nalla, A. P. Tomsia, *Science* 2006, *311*, 515.**

[83] **Z. Tang, N. A. Kotov, S. Magonov, B. Ozturk, *Nat. Mater.* 2003, *2*, 413.**

[84] **L. J. Bonderer, A. R. Studart, L. J. Gauckler, *Science* 2008, *319*, 1069.**

[85] **A. Walther, I. Bjurhager, J. M. Malho, J. Pere, J. Ruokolainen, L. A. Berglund, O. Ikkala, *Nano Lett.* 2010, *10*, 2742.**

[86] **H. B. Yao, Z. H. Tan, H. Y. Fang, S. H. Yu, *Angew. Chem. Int. Ed.* 2010, *49*, 10127.**

[87] **T. Kato, *Adv. Mater.* 2000, *12*, 1543.**

[88] **R. A. MacDonald, B. F. Laurenzi, G. Viswanathan, P. M. Ajayan, J. P. Stegemann, *J. Biomed. Mater. Res. Part A* 2005, *74A*, 489.**

[89] **J. F. Wang, Q. F. Cheng, Z. Y. Tang, *Chem. Soc. Rev.* 2012, *41*, 1111.**

[90] **P. Podsiadlo, A. K. Kaushik, E. M. Arruda, A. M. Waas, B. S. Shim, J. Xu, H. Nandivada, B. G. Pumplin, J. Lahann, A. Ramamoorthy, N. A. Kotov, *Science* 2007, *318*, 80.**

[91] L. Wågberg, G. Decher, M. Norgren, T. Lindström, M. Ankerfors, K. Axnäs, *Langmuir* 2008, *24*, 784.

[92] C. N. Wu, T. Saito, S. Fujisawa, H. Fukuzumi, A. Isogai, *Biomacromolecules* 2012, *13*, 1927.

[93] P. Laaksonen, A. Walther, J. M. Malho, M. Kainlauri, O. Ikkala, M. B. Linder, *Angew. Chem. Int. Ed.* 2011, *50*, 8688.

[94] M. Wang, A. Olszewska, A. Walther, J. M. Malho, F. H. Schacher, J. Ruokolainen, M. Ankerfors, J. Laine, L. A. Berglund, M. Osterberg, O. Ikkala, *Biomacromolecules* 2011, *12*, 2074.

[95] M. Kettunen, R. J. Silvennoinen, N. Houbenov, A. Nykanen, J. Ruokolainen, J. Sainio, V. Pore, M. Kemell, M. Ankerfors, T. Lindstrom, M. Ritala, R. H. A. Ras, O. Ikkala, *Adv. Funct. Mater.* 2011, *21*, 510.

[96] P. Fratzl, *Curr. Opin. Colloid Interface Sci.* 2003, *8*, 32.

Aalto-DD 154/2012

ISBN 978-952-60-4874-1
ISBN 978-952-60-4875-8 (pdf)
ISSN-L 1799-4934
ISSN 1799-4934
ISSN 1799-4942 (pdf)

Aalto University
School of Science
Department of Applied Physics
www.aalto.fi

BUSINESS +
ECONOMY

ART +
DESIGN +
ARCHITECTURE

SCIENCE +
TECHNOLOGY

CROSSOVER

**DOCTORAL
DISSERTATIONS**